

3-26-2015

## **Analysis of the Nuclear Structure of Rhenium-186 Using Neutron-Induced Reactions**

David A. Matters

Follow this and additional works at: <https://scholar.afit.edu/etd>

---

### **Recommended Citation**

Matters, David A., "Analysis of the Nuclear Structure of Rhenium-186 Using Neutron-Induced Reactions" (2015). *Theses and Dissertations*. 85.  
<https://scholar.afit.edu/etd/85>

---

This Thesis is brought to you for free and open access by the Student Graduate Works at AFIT Scholar. It has been accepted for inclusion in Theses and Dissertations by an authorized administrator of AFIT Scholar. For more information, please contact [AFIT.ENWL.Repository@us.af.mil](mailto:AFIT.ENWL.Repository@us.af.mil).



**Analysis of the Nuclear Structure of  $^{186}\text{Re}$  Using  
Neutron-Induced Reactions**

THESIS

David A. Matters, Major, USA  
AFIT-ENP-MS-15-M-098

**DEPARTMENT OF THE AIR FORCE  
AIR UNIVERSITY**

**AIR FORCE INSTITUTE OF TECHNOLOGY**

**Wright-Patterson Air Force Base, Ohio**

DISTRIBUTION STATEMENT A  
APPROVED FOR PUBLIC RELEASE; DISTRIBUTION UNLIMITED

The views expressed in this document are those of the author and do not reflect the official policy or position of the United States Air Force, the United States Army, the United States Department of Defense or the United States Government. This material is declared a work of the U.S. Government and is not subject to copyright protection in the United States.

AFIT-ENP-MS-15-M-098

ANALYSIS OF THE NUCLEAR STRUCTURE OF  $^{186}\text{RE}$  USING  
NEUTRON-INDUCED REACTIONS

THESIS

Presented to the Faculty  
Department of Engineering Physics  
Graduate School of Engineering and Management  
Air Force Institute of Technology  
Air University  
Air Education and Training Command  
in Partial Fulfillment of the Requirements for the  
Degree of Master of Science

David A. Matters, BA, MA, MBA  
Major, USA

March 2015

DISTRIBUTION STATEMENT A  
APPROVED FOR PUBLIC RELEASE; DISTRIBUTION UNLIMITED

AFIT-ENP-MS-15-M-098

ANALYSIS OF THE NUCLEAR STRUCTURE OF  $^{186}\text{RE}$  USING  
NEUTRON-INDUCED REACTIONS

THESIS

David A. Matters, BA, MA, MBA  
Major, USA

Committee Membership:

Dr. J. W. McClory  
Chair

Dr. J. J. Carroll  
Member

LTC S. R. McHale, PhD  
Member

## Abstract

Evaluated nuclear data for  $^{186}\text{Re}$  identify the majority of spin-parity assignments as tentative, with approximate values for the energies of several levels and transitions. In particular, the absence of known transitions that feed the  $J^\pi = 8^+$  isomer  $^{186m}\text{Re}$  motivates their discovery. This isomer, which has a half life of  $2 \times 10^5$  years, has a potential application in an isomer power source. Additionally, the isomer's role in certain nucleosynthesis processes is not well understood, so measured cross sections for transitions that feed the isomer would have astrophysical implications. Using the GErmanium Array for Neutron Induced Excitations (GEANIE) spectrometer at the Los Alamos Neutron Science Center (LANSCE),  $(n, 2n\gamma)$  and  $(n, n'\gamma)$  reactions in a 99.52% enriched  $^{187}\text{Re}$  target were used to obtain  $\gamma$ -ray spectra from  $^{186}\text{Re}$  and  $^{187}\text{Re}$ , respectively. The experimental data reveal 5 new transitions in  $^{186}\text{Re}$  and 4 new transitions in  $^{187}\text{Re}$ . Similarities between the level schemes of  $^{184}\text{Re}$  and  $^{186}\text{Re}$  suggest that one of the newly-observed transitions in  $^{186}\text{Re}$  feeds the isomer from a level at 414.9 keV. The  $\gamma$ -ray energy measured for this transition implies an isomer energy of 148.2(5) keV, which is a significant improvement over the adopted value of 149(7) keV.

*To Megan and Xavier*

## Acknowledgements

I would like to thank Dr. John McClory for granting me the support and autonomy necessary to take on this project. His encouragement and advocacy in extending me to the Ph.D. program in Applied Physics at AFIT has opened the door for me to pursue my lifelong dream of becoming a physicist. I am very grateful to Dr. Jeff Carroll of the Army Research Laboratory (ARL) for his mentorship and instruction in nuclear physics, the subject that I am most passionate about. I consider myself very fortunate to have the opportunity to partake in experiments that he has been instrumental in setting up. Thanks to LTC Stephen McHale for his support, instruction and the example of professionalism he set for all the officers in the nuclear engineering program. Thanks also to Dr. Chris Chiara of ARL and Oak Ridge Associated Universities for his assistance during the experiment and help with spectral analysis software. This thesis research could not have happened without the experimental expertise of Drs. Nikolaos Fotiades, Matt Devlin and Ron Nelson of Los Alamos Neutron Science Center (LANSCE). I am thankful for their guidance during the experiment and afterwards with the data analysis. The experiment was performed using the LANSCE accelerator facility at Los Alamos National Laboratory, supported under contract DE-AC52-06NA25396, with target samples purchased by ARL and travel funded by the Defense Threat Reduction Agency and the Domestic Nuclear Detection Office of the Department of Homeland Security.

David A. Matters

## Table of Contents

	Page
Abstract . . . . .	iv
Acknowledgements . . . . .	vi
List of Figures . . . . .	ix
List of Tables . . . . .	xi
I. Introduction . . . . .	1
1.1 Background . . . . .	1
1.2 Motivation . . . . .	1
1.3 Problem . . . . .	4
1.4 Hypothesis . . . . .	5
1.5 Methods . . . . .	6
II. Theory . . . . .	7
2.1 Nuclear Landscape . . . . .	7
2.2 Microscopic Models . . . . .	8
2.3 Collective Models . . . . .	17
2.4 Combined Models . . . . .	18
2.5 Metastable Excited States (Isomers) . . . . .	19
2.6 Neutron-Induced Excitations . . . . .	24
2.7 Literature Review . . . . .	27
III. Experiment . . . . .	30
3.1 Experimental Facilities . . . . .	30
3.2 Target Sample Preparation . . . . .	37
3.3 Experiment Summary . . . . .	39
IV. Results and Analysis . . . . .	43
4.1 Data Acquisition and Online Analysis . . . . .	43
4.2 Offline Data Analysis Methodology . . . . .	45
4.3 Projection Spectrum Analysis . . . . .	54
4.4 $\gamma - \gamma$ Coincidence Matrix Analysis . . . . .	63
4.5 New $\gamma$ -ray Transitions in $^{187}\text{Re}$ . . . . .	64
4.6 New $\gamma$ -ray Transitions in $^{186}\text{Re}$ . . . . .	66

	Page
V. Future Work . . . . .	70
5.1 Excitation Functions . . . . .	70
5.2 Transition Cross Section Calculations . . . . .	70
5.3 Reaction Modeling . . . . .	74
5.4 Examination of Data from $^{nat}\text{Re}$ Runs . . . . .	75
VI. Conclusion . . . . .	78
6.1 Contributions to the Level Schemes of $^{187}\text{Re}$ and $^{186}\text{Re}$ . . . . .	78
6.2 Improved Estimate of $^{186m}\text{Re}$ Energy . . . . .	79
6.3 Recommendations for Future Research . . . . .	79
Appendix A. Photoexcitation of $^{115m}\text{In}$ Using a Dynamitron Accelerator . . . . .	80
1.1 Introduction . . . . .	81
1.2 Hypothesis . . . . .	83
1.3 Experiment . . . . .	84
1.4 Modeling Approach . . . . .	90
1.5 Results and Analysis . . . . .	92
1.6 Conclusion . . . . .	94
Bibliography . . . . .	96
Vita . . . . .	99

## List of Figures

Figure	Page
1 Processes involved in the nucleosynthesis of rhenium and osmium .....	3
2 Extract from the low-energy level scheme of $^{186}\text{Re}$ .....	5
3 Chart of the nuclides .....	8
4 Nuclear shell model with spin-orbit interaction .....	10
5 Shapes of deformed nuclei .....	14
6 Nilsson diagrams for neutron and proton levels .....	15
7 Definition of quantum number $K$ in the Nilsson model .....	16
8 Single nucleon orbits in the Nilsson model .....	16
9 Vibrational modes in deformed nuclei .....	18
10 Excitation energy versus spin and $K$ in spin trap and $K$ -trap isomers .....	21
11 Isomer depletion and photoexcitation schemes .....	22
12 Cross sections for $(n, xn)$ reactions in $^{187}\text{Re}$ .....	26
13 Extract from $^{186}\text{Re}$ level scheme showing particle configurations .....	28
14 LANSCE/WNR facility diagram .....	31
15 Neutron flux spectra for LANSCE/WNR target 4 flight paths .....	32
16 Schematic of the LANSCE/WNR 4FP60R flight path and GEANIE array .....	33
17 GEANIE detector array .....	34
18 GEANIE HPGe detector positions .....	35
19 Rhenium target holder .....	38
20 Data acquisition and transfer flow chart .....	43

Figure	Page
21 Data analysis methodology flow chart .....	48
22 Time spectra and TOF to neutron energy correspondence .....	50
23 Summed planar detector spectrum .....	55
24 Summed coaxial detector spectrum.....	58
25 Extracts from the $^{184}\text{Re}$ and $^{186}\text{Re}$ level schemes .....	67
26 Low-energy level scheme for $^{115}\text{In}$ .....	82
27 Dynamitron sample positioning .....	85
28 CASINO simulation output for WSU/AFIT experiment.....	86
29 Canberra HPGe detector efficiency calibration .....	88
30 Hourly irradiated indium counts from WSU/AFIT experiment .....	89
31 HPGe spectra from ARL and WSU/AFIT experiments .....	90
32 Modeled spectral flux densities for ARL and WSU/AFIT experiments .....	93

## List of Tables

Table		Page
1	GEANIE detector a positions .....	36
2	Peaks in planar detector spectrum, $^{187}\text{Re}(n, n'\gamma)^{187}\text{Re}$ reaction channel .....	56
3	Peaks in planar detector spectrum, $^{187}\text{Re}(n, 2n\gamma)^{186}\text{Re}$ reaction channel .....	57
4	Peaks in coaxial detector spectrum, $^{187}\text{Re}(n, n'\gamma)^{187}\text{Re}$ reaction channel .....	59
5	Peaks in coaxial detector spectrum, $^{187}\text{Re}(n, 2n\gamma)^{186}\text{Re}$ reaction channel .....	60
6	Energies of X-rays evident in $\gamma$ -ray spectra .....	61
7	Low-energy intermediate states for photoexcitation of $^{115m}\text{In}$ .....	82

# ANALYSIS OF THE NUCLEAR STRUCTURE OF $^{186}\text{Re}$ USING NEUTRON-INDUCED REACTIONS

## I. Introduction

### 1.1 Background

Natural rhenium consists of 37.4%  $^{185}\text{Re}$  and 62.6%  $^{187}\text{Re}$ . It was the last stable element to be discovered, and it is notable for the fact that it has the highest boiling point and the third highest melting point of all elements. These physical properties make rhenium suitable as a coating for turbine blades used in aircraft jet engines. Due to its demand in the aerospace industry and its rarity, samples of rhenium metal can be very expensive [1].

The isotope  $^{186}\text{Re}$  can be created by neutron capture ( $n, \gamma$ ) on  $^{185}\text{Re}$  or by ( $n, 2n$ ) reactions from  $^{187}\text{Re}$ , and is unstable in its ground state. In the ground state,  $^{186}\text{Re}$  decays via electron capture or  $\beta^-$  decay with a half life of 2.718 days, but  $^{186}\text{Re}$  also has an unusually long-lived metastable state, or isomer. The isomer  $^{186m}\text{Re}$  has a half-life of  $2.0 \times 10^5$  years and decays via  $\gamma$ -ray cascade to the ground state [2].

### 1.2 Motivation

The motivators for research on the nuclear structure of  $^{186}\text{Re}$  are (1) addressing a long-standing astrophysical question related to the rhenium/osmium cosmochronometer, and (2) developing a radioisotope power source for use on the battlefield.

## Re-Os Cosmochronometer.

The isotope  $^{187}\text{Re}$  has a half-life in its ground state of  $4.35 \times 10^{10}$  years [2], and it  $\beta^-$  decays to the stable isotope  $^{187}\text{Os}$ . The long half-life of  $^{187}\text{Re}$ , on the order of the age of the universe ( $15 \pm 2$  Gyr) makes the  $^{187}\text{Re}/^{187}\text{Os}$  system suitable as a chronometer with which one can estimate the ages of astronomical objects.

Measurement of the relative abundances of  $^{187}\text{Re}$  and  $^{187}\text{Os}$  in meteorites permits one to date the nucleosynthesis of rhenium and osmium by high neutron flux events such as supernovae. The Re-Os radioactive decay system has been proposed as a mechanism by which one can determine the age of the galaxy [3].

The nucleosynthesis of  $^{187}\text{Re}$  and  $^{187}\text{Os}$  involves both a rapid  $r$ -process, and a slow  $s$ -process. In the  $r$ -process, neutron fluxes in the stellar environment are so high that unstable isotopes have a high probability of undergoing neutron capture before they have the opportunity to  $\beta$  decay, while in the  $s$ -process neutron capture rates are low enough that  $\beta$  decay plays an appreciable role. These processes, shown in Figure 1, result in the production of  $^{187}\text{Os}$  almost entirely by  $s$ -process and  $^{187}\text{Re}$  mostly by  $r$ -process. In this scheme,  $^{186}\text{Re}$  is considered a branch point, in that it can decay with a half-life of 3.72 days into  $^{186}\text{Os}$  or undergo neutron capture to create  $^{187}\text{Re}$  [4, 5, 6]. Consideration of the role of the  $^{186m}\text{Re}$  isomer (which is not known to  $\beta^-$  decay independently) in this process would reduce errors inherent in the use of  $^{187}\text{Re}/^{187}\text{Os}$  as an effective chronometer [7]. Due to its  $2.0 \times 10^5$  year half-life,  $^{186m}\text{Re}$  exists long enough to dramatically increase the chance of neutron capture over  $\beta^-$  decay, thus increasing the rate of production of  $^{187}\text{Re}$ . It is possible that the  $^{186m}\text{Re}$  isomer could be created through neutron-induced reactions in a stellar environment, which motivates the discovery of transitions that feed the isomer and experimental determination of their associated cross sections.

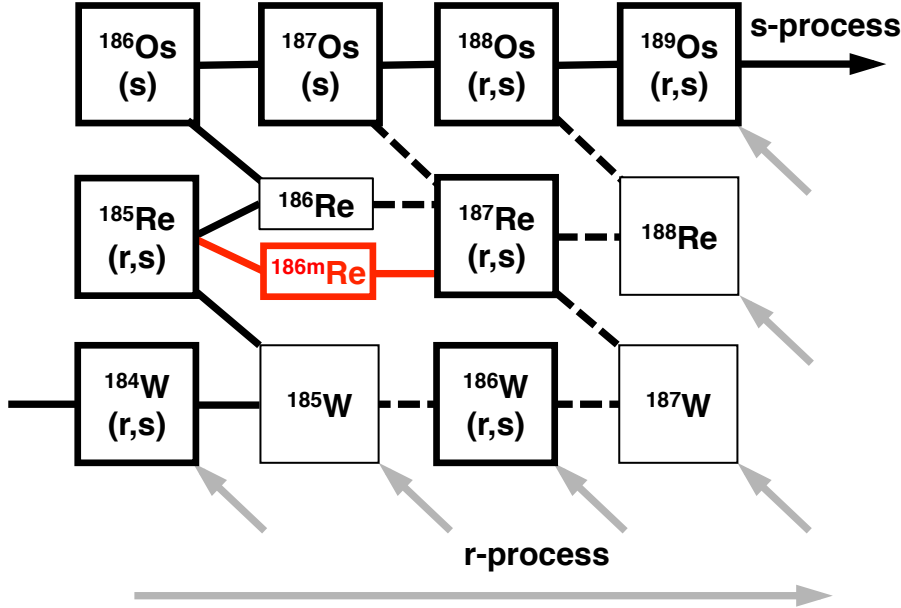


**Figure 1.** Rapid (*r*, gray arrows) and slow (*s*, solid black line) processes involved in the production of  $^{187}\text{Re}$  and  $^{187}\text{Os}$ . Long-lived nuclides are identified with bold boxes, with the dashed lines indicating weak, or secondary processes. The red outline around the isomer  $^{186m}\text{Re}$  and associated pathways highlights the fact that its role in these processes is not yet understood.

### Isomer Power Source.

Long-lived nuclear isomers store up to  $10^6$  times more energy per gram of material than chemical energy sources. These isomers release their excess energy through a variety of decay mechanisms, with half-lives ranging from milliseconds to thousands of years. If the isomer decays directly to the ground state, the released energy is not a product of the binding energy of the nucleus, so it does not involve transmutation. As a result, the significant amounts of radioactive waste produced by nuclear fission in the form of fission fragments and neutron activation products are not present following the decay of nuclear isomers. Several methods, including X-ray irradiation and neutron bombardment, have been shown to induce depletion of certain isomers as a means of accessing their stored excitation energy. However, the goal of inducing a nucleus to release energy on demand in practical quantities

remains elusive [8].

As technology on the battlefield becomes more advanced, forward-deployed military forces require increasingly powerful energy sources to operate equipment. The portability of these power sources can have a critical effect on mission readiness, so high energy density sources such as nuclear isomers are of particular interest. To highlight the importance of this goal, the Defense Science Board in its October 2013 report recommended that \$25 million be allocated to research relating to the development of a radioisotope power source [9]

$^{186m}\text{Re}$ , given its half-life of  $2.0 \times 10^5$  years, has the advantage of being a stable energy storage medium. If  $^{186m}\text{Re}$  could be transformed from the isomer to the ground state of  $^{186}\text{Re}$  on demand, the ground state would then  $\beta^-$  decay to  $^{186}\text{Os}$  with a half-life of 3.7 days, producing electrons with energies up to 1.08 MeV. In one possible radioisotope power source design, the energetic electrons could produce scintillation light in a crystal that could in turn generate an electric current using a photovoltaic cell.

Identifying transitions in the nuclear structure of  $^{186}\text{Re}$  that feed the isomer could lead to the discovery of a method for inducing depletion of  $^{186m}\text{Re}$ . The potential of nuclear isomers as a power source was outlined by P. Walker and J. J. Carroll, in which photon-induced depletion of isomers was proposed as a means of achieving on-demand energy release [8]. The ultimate goal of these types of isomer depletion experiments is the discovery of a mechanism by which the isomeric state can be depleted with a favorable energy balance.

### 1.3 Problem

The objective of this research was to conduct an examination of the nuclear level structure of  $^{186}\text{Re}$ , with the specific goal of discovering transitions that feed the

149(7) keV isomer.  $^{186}\text{Re}$  is an isotope with a relatively poorly known structure. A search of the Evaluated Nuclear Structure Data File (ENSDF) for  $^{186}\text{Re}$  identifies the majority of spin-parity assignments as tentative, with approximate values associated with the energies of several levels and transitions, as shown in Figure 2. Of note in Figure 2 is the absence of known transitions that populate the  $^{186m}\text{Re}$  isomer.

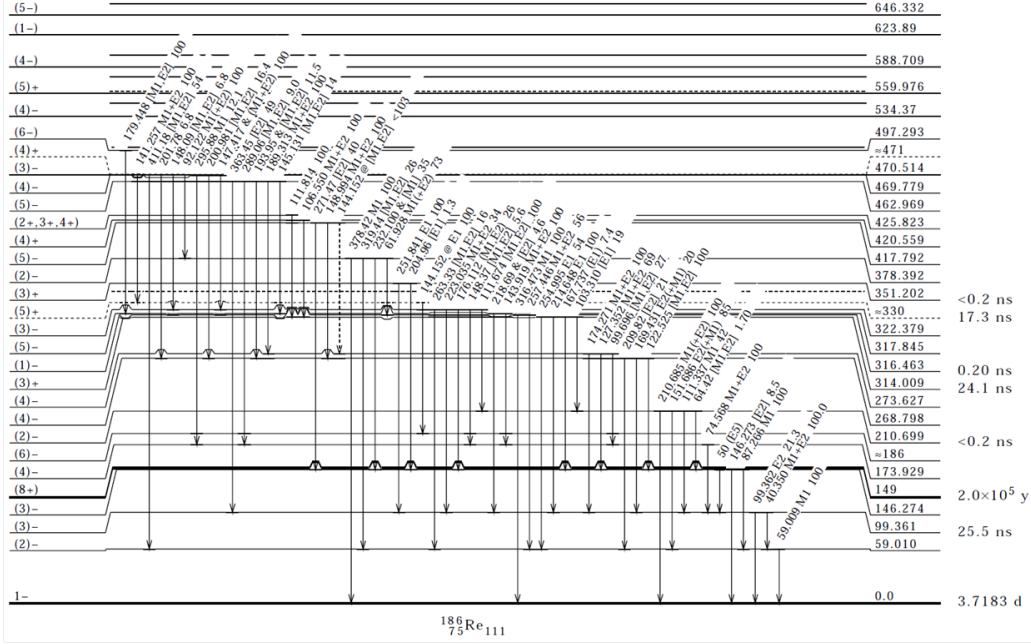


Figure 2. An extract from the low-energy level scheme of  $^{186}\text{Re}$  shows that there are numerous levels for which the multipolarity is identified with parentheses as tentative, while transitions and energies assigned to several levels are approximate [10].

## 1.4 Hypothesis

Measurements of  $\gamma$ -ray spectra from the reaction  $^{187}\text{Re}(n, 2n\gamma)^{186}\text{Re}$  would provide valuable input to nuclear structure databases such as the Experimental Unevaluated Nuclear Data List (XUNDL) and the Evaluated Nuclear Structure Data File (ENSDF). New levels and transitions discovered in  $^{186}\text{Re}$ , and in particular levels that directly populate the  $^{186m}\text{Re}$  isomer, would help solve the

problems identified in Section 1.2.

## 1.5 Methods

Using the GErmanium Array for Neutron Induced Excitations (GEANIE) detector array at the Los Alamos Neutron Science Center (LANSCE) Weapons Neutron Research (WNR) facility,  $\gamma$ -ray spectra obtained from neutron-induced reactions were used to identify new  $\gamma$ -ray transitions in  $^{186}\text{Re}$  and verify transitions and levels already described in existing literature. The primary neutron-induced reaction studied was  $^{187}\text{Re}(n, 2n\gamma)^{186}\text{Re}$ , from irradiating a rhenium powder sample enriched in  $^{187}\text{Re}$ . The isotope  $^{184}\text{Re}$  has a similar structure to  $^{186}\text{Re}$ , so known  $\gamma$ -ray transitions in  $^{184}\text{Re}$  were used as a guide to identifying transitions feeding the isomer in  $^{186}\text{Re}$ .

## II. Theory

The physics of nuclear structure, which is concerned with the levels and transitions in nuclei at excitation energies below approximately 2-3 MeV, incorporates both collective and microscopic models of nucleon motion [11]. Both are important to understanding the structure of nuclei with odd numbers of protons and neutrons, such as  $^{186}\text{Re}$ .

### 2.1 Nuclear Landscape

The observed instability of radioisotopes provided the first clues to understanding the physics underlying nuclear structure. In a plot of the atomic number  $Z$  versus the neutron number  $N$  of known isotopes (Figure 3), a clear valley of stable nuclei emerges, with unstable neutron-rich isotopes below the valley and unstable proton-rich isotopes above it. The shape of this valley led to the development of the first successful macroscopic, or collective, model of nuclear structure, known as the liquid drop model (discussed further in Section 2.3).

Certain nuclei, with values of  $N$  or  $Z$  equal to the so-called magic numbers, are known to be especially stable, a behavior not predicted by collective models. The magic numbers,  $N, Z = 2, 8, 20, 28, 50, 82, 126$ , are shown, except for  $N, Z = 2$ , in Figure 3. Gaps are also observed at  $N, Z = 40$  (not identified in the figure) and  $Z = 64$  for certain  $N$  [13]. Evidence of the stability of nuclei with magic  $N$  or  $Z$  values led to the development of the nuclear shell model, a microscopic model that treats the neutrons and protons in the nucleus individually instead of collectively.

The shell model assumes a spherical nuclear potential, limiting its applicability in some cases where the nucleus has a non-spherical shape. This modification to the shell model, known as the Nilsson model, takes into account the deformation of the

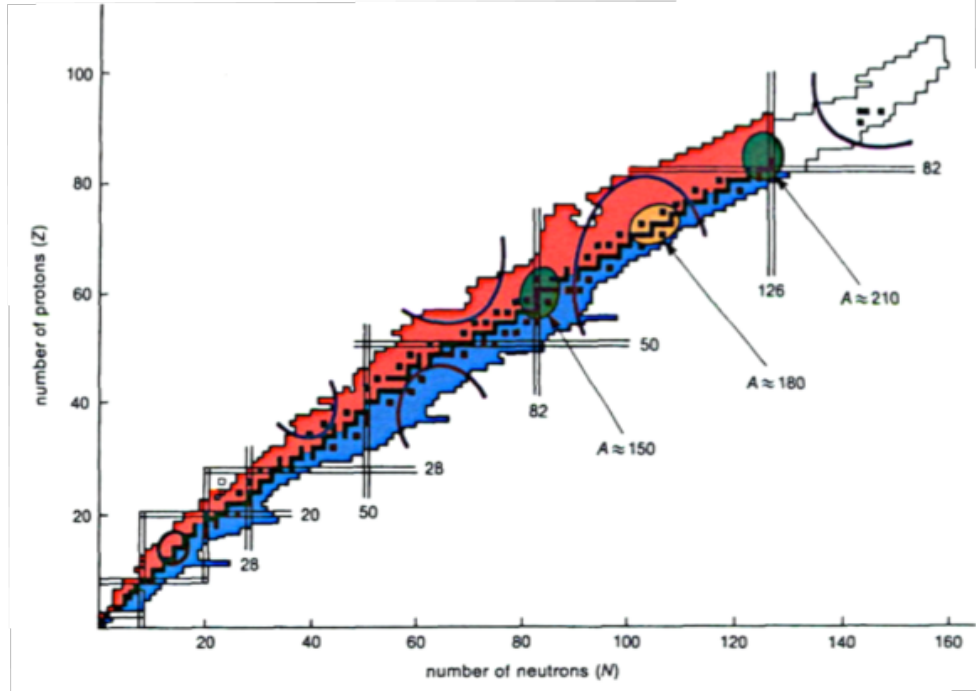


**Figure 3.** The chart of the nuclides, showing the rough valley of stable nuclei (black dots) in the center of the plot of proton number  $Z$  versus neutron number  $N$ . Magic numbers are identified by double lines, while realms in which nuclear deformation is significant are outlined in purple arcs. The most common locations in which spin-trap isomers are found are highlighted in green, while  $K$ -trap isomers are generally found in the area highlighted in orange. Figure copyright 1994, IOP Publishing. Reproduced with permission from [12].

nucleus in predicting nuclear behavior. The realms in which nuclear deformation effects are significant are shown as circles or arcs in Figure 3. Of note,  $^{186}\text{Re}$ , the nucleus studied in this work, falls well within the mid-shell region with  $82 < N < 126$  and  $50 < Z < 82$ , where deformation is a contributing factor.

## 2.2 Microscopic Models

Microscopic models of the nucleus are concerned with the behavior of individual nucleons and their effects on the stability of the nucleus. A number of microscopic models exist, the most successful of which has been the nuclear shell model [13].

## Shell Model.

The nuclear shell model (with spin-orbit coupling) provides a basis for understanding the behavior of nuclear excited states. In this basic model, which assumes a spherical nuclear potential, protons and neutrons are assumed to be independent particles, each occupying distinct shells in accordance with the Pauli exclusion principle. When spin-orbit coupling is included in the model, the resulting predictions of nuclear stability are in relatively close agreement with experiment. In particular, the shell model exactly predicts the experimentally observed magic numbers, and it also predicts that  $N, Z = 184$  is magic in the absence of empirical evidence [14]. The individual particle levels predicted by the shell model are shown in Figure 4, in which each level is identified by its angular momentum quantum number  $\ell$ , with  $s, p, d, \dots$  referring to  $\ell = 0, 1, 2, \dots$ . The capacity of a particular level is shown to the right of the level, and to the far right is the cumulative number of nucleons in that level and all lower levels.

The shell model can be used to explain behavior seen in nuclear level schemes. As an example, consider nuclei with both  $N$  and  $Z$  magic. Level schemes for these doubly magic nuclei show a large energy gap between the ground state and the first excited state, which is explained by the fact that a significant amount of energy is required to promote a nucleon out of a closed shell to the next (empty) shell. Application of the shell model to the case of nuclei away from closed shells requires the independent particle approximation, discussed in greater detail in Section 2.4.

Transition rates between states reflect the stability of each state and are governed by quantum mechanical selection rules. Gamma rays, which result from transitions between energy levels, are electromagnetic radiation with characteristic multipolarity (i.e.,  $M1$ ,  $E2$ , etc.). Quantum mechanical calculations of the transition probabilities include the following selection rules for transitions between

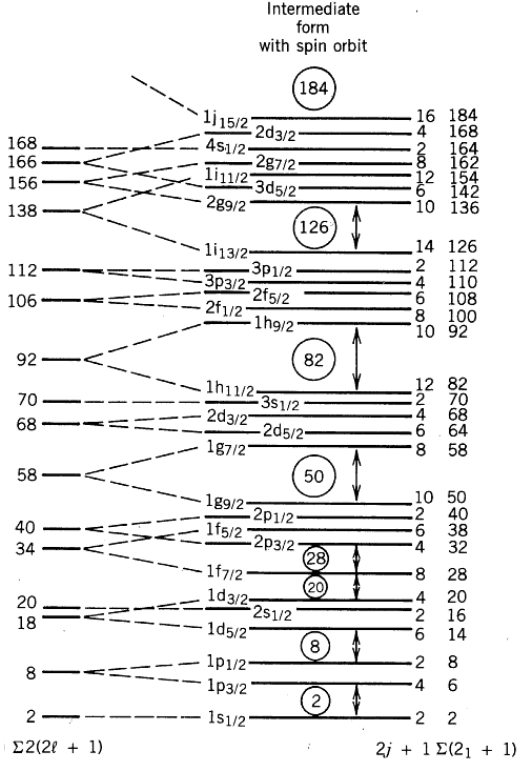


**Figure 4.** Energy levels of the nuclear shell model (including spin-orbit interaction). The magic numbers, corresponding to completely filled nuclear shells, are identified with circles. Reproduced with permission from [14].

energy levels:

$$|\ell_i - \ell_f| \leq L \leq \ell_i + \ell_f$$

$$\Delta\pi = -1 \rightarrow \text{even electric, odd magnetic} \quad (1)$$

$$\Delta\pi = +1 \rightarrow \text{odd electric, even magnetic.}$$

Here  $L$  is the multipole order ( $L > 0$ ) of the electromagnetic transition,  $\ell_i$  and  $\ell_f$  are the angular momentum quantum numbers of the initial and final states. The change in parity  $\Delta\pi$  between initial and final states is equal to  $+1$  if there is no change in parity and  $-1$  for a change in parity. For given initial and final states, multiple transition multipolarities may be possible, in which case the most likely

transition is the one with the lowest multipole order. For a given multipole order, electric transitions are more likely than magnetic ones. These effects are revealed quantitatively by the Weisskopf estimates.

### Weisskopf Estimates.

The Weisskopf estimates, which arise from calculations of radial transition matrix elements, provide a first-order approximation of the transition rates between nuclear states [11, 14]. These estimates are based on the assumption of a particularly simple spherical potential, so they are directly applicable only to the case of spherical nuclear states. Even in this limited case they predict rates that can result in order of magnitude differences from measured decay rates.

Given the atomic number  $A$  and the observed transition energy  $E$  in MeV, the Weisskopf estimates give the transition rate  $\lambda$  in units of  $s^{-1}$ . For electric transitions  $E1$  through  $E4$  (dipole through hexadecapole), they are:

$$\begin{aligned}\lambda(E1) &= 1.0 \times 10^{14} A^{2/3} E^3 \\ \lambda(E2) &= 7.3 \times 10^7 A^{4/3} E^5 \\ \lambda(E3) &= 34 A^2 E^7 \\ \lambda(E4) &= 1.1 \times 10^{-5} A^{8/3} E^9.\end{aligned}\tag{2}$$

For magnetic transitions, the Weisskopf estimates for the  $M1$  through  $M4$

transition rates are:

$$\begin{aligned}\lambda(M1) &= 5.6 \times 10^{13} E^3 \\ \lambda(M2) &= 3.5 \times 10^7 A^{2/3} E^5 \\ \lambda(M3) &= 16 A^{4/3} E^7 \\ \lambda(M4) &= 4.5 \times 10^{-6} A^2 E^9.\end{aligned}\tag{3}$$

It is important to note that the leading constant in these estimates decreases by approximately 6 orders of magnitude for each incremental increase in multipole order. The transition rate also depends on the energy of the transition. As transition energy  $E$  increases, the transition rate increases as  $E^{2L+1}$ , where  $L$  is the multipole order of the transition [11, 14].

### **Deformed Shell Model.**

The shell model has proven itself an incredibly powerful tool with which one can explain many aspects of nuclear behavior, including excited state energy levels and transition rates. These predictions agree relatively well with experiment for nuclei with  $N$  or  $Z$  close to the magic numbers, where nuclei are spherical in their ground state. However, as mentioned in Section 2.1, the shell model applies directly only when the nuclear potential can be reasonably approximated as spherical. Nuclei in the mid-shell range with mass  $150 \leq A \leq 190$  are generally non-spherical, so the spherical potential approximation used in the derivation of the nuclear shell model is flawed.

The two symmetries encountered in deformed nuclei are oblate (frisbee) and prolate (football) shapes, with the up direction aligned with the axis of rotation (by convention, the  $z$ -axis in the center-of-mass reference frame). That is, an oblate

nucleus extends further in the equatorial direction than in the polar direction, and the opposite is true for a prolate nucleus.

For a purely spherical nucleus, the nuclear radius  $R$  is given by

$$R = R_0 A^{1/3}, \quad (4)$$

where  $A = N + Z$  is the mass number and  $R_0 = 1.2$  fm. For a non-spherical nucleus with a static quadrupole deformation, the nuclear radius becomes

$$R = R_0 A^{1/3} \left[ 1 + \sum_{\mu} \alpha_{2\mu}^* Y_{2\mu}(\theta, \phi) \right], \quad (5)$$

where the  $\alpha_{2\mu}$  are the (quadrupole) expansion coefficients for the spherical harmonics  $Y_{2\mu}(\theta, \phi)$  [11, 13]. In the center-of-mass reference frame, the expansion coefficients  $\alpha_0, \alpha_{\pm 2}$  can be written in terms of a deformation parameter  $\beta$  and an angle  $\gamma$  as  $\alpha_0 = \beta \cos \gamma$  and  $\alpha_{\pm 2} = \frac{1}{\sqrt{2}} \beta \sin \gamma$ . The parameter  $\beta$  specifies the shape of the distortion of the nucleus, with  $\beta < 0$  for an oblate nucleus and  $\beta > 0$  for a prolate nucleus. The angle  $\gamma$  is a measure of the axial asymmetry of the nucleus, ranging from  $\gamma = 0^\circ$  for an axially symmetric nucleus to  $\gamma = 30^\circ$ , which corresponds to the case of maximum axial asymmetry [11, 13]. The diagram in Figure 5 shows the equipotential surfaces for each of the shapes described above.

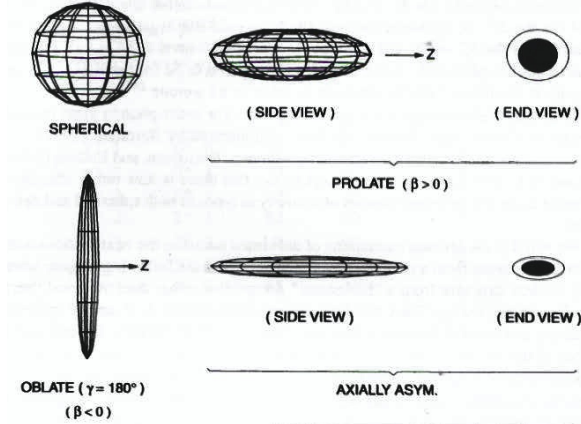


**Figure 5.** Characteristic shapes of equipotential surfaces in deformed nuclei. The spherical shape has  $\beta = 0$ , while the oblate and prolate shapes have  $\beta < 0$  and  $\beta > 0$ , respectively. The axial symmetry is a function of  $0^\circ \leq \gamma \leq 30^\circ$ , and the end views show different degrees of axial asymmetry for the prolate and oblate shapes. Reproduced with permission from [13].

A more accurate model of the nucleus is based on this deformed potential, in which the degree of deformation  $\epsilon$  is accounted for in determining the energy levels. The degree of deformation  $\epsilon$  is a function of the deformation parameter  $\beta$  according to the relation

$$\beta = \sqrt{\pi/5} \left( \frac{4}{3}\epsilon + \frac{4}{9}\epsilon^2 + \frac{4}{27}\epsilon^3 + \frac{4}{81}\epsilon^4 + \dots \right). \quad (6)$$

The deformed shell model, also known as the Nilsson model, accounts for the non-spherical nature of mid-shell nuclei [2]. The resulting energy levels show significant dependence on the deformation, which is evident in the so-called Nilsson diagram of Figure 6. For  $^{186}\text{Re}$ ,  $\beta = 0.22$ , which corresponds to  $\epsilon = 0.194$  per Equation 6 [15].

In the Nilsson model, the energy levels of deformed nuclei depend on the projection of the angular momentum on the axis of symmetry, defined as the quantum number  $K$  as shown in Figure 7. Levels in the Nilsson model are identified according to the convention  $K^\pi [Nn_z\Lambda]$ . The first quantum numbers  $K^\pi$  define the  $K$  value and parity of the state,  $N$  represents the principle quantum number which

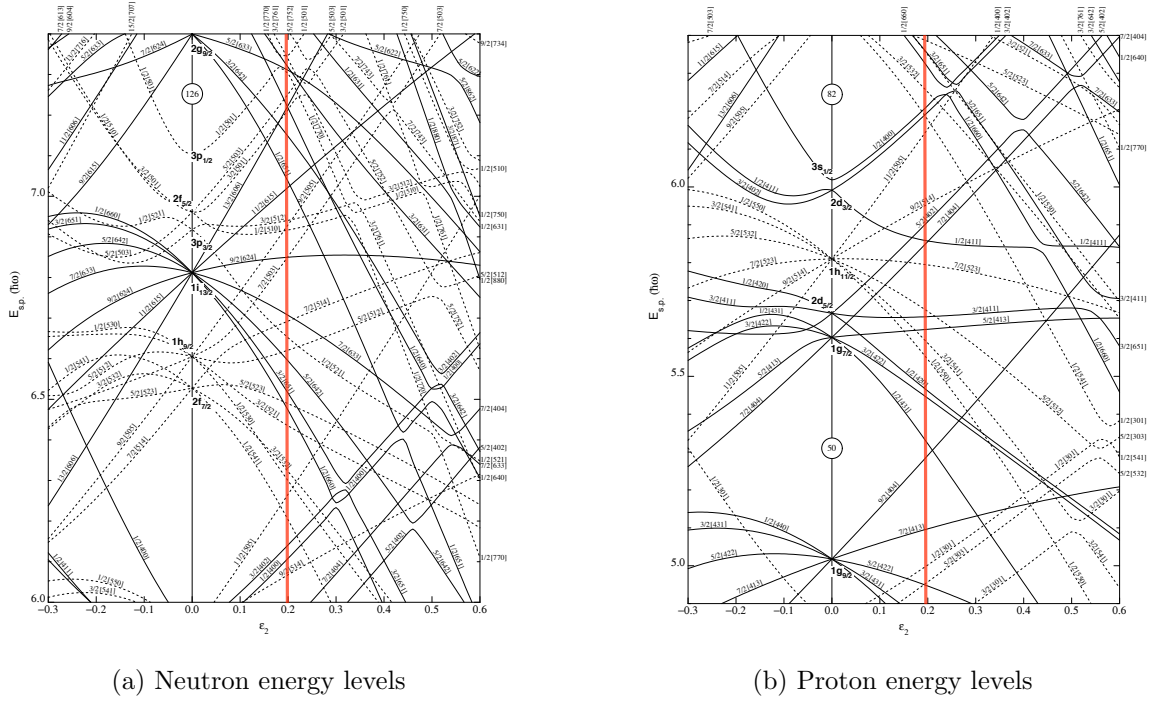


**Figure 6.** Deformed shell model (Nilsson) energy level diagrams for (a) neutrons and (b) protons in deformed nuclei with  $82 \leq N \leq 126$  and  $50 \leq Z \leq 82$ . The parameter  $\epsilon$  ( $\epsilon_2$  in the figure) is a measure of the deformation of the nucleus:  $\epsilon < 0$  for oblate nuclei and  $\epsilon > 0$  for prolate nuclei. The vertical red line identifies the value of  $\epsilon = 0.195$  for  $^{186}\text{Re}$ . Magic numbers are identified by circles. Figure copyright 2009 Wiley-VCH Verlag GmbH & Co. KGaA. Reproduced with permission from [2].

defines the major shell, and  $n_z$  is the number of modes of the wavefunction in the  $z$  direction. The quantum number  $\Lambda$  is the component of the orbital angular momentum along the symmetry axis. Using these definitions, for a nucleon with spin  $1/2$  and a spin projection  $\Sigma = \pm 1/2$  on the nuclear symmetry axis, the  $K$  value is equal to  $\Lambda + \Sigma$ .

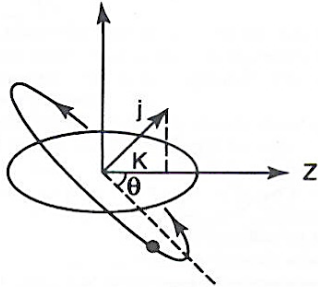


**Figure 7.** Definition of quantum number  $K$  and angle of inclination  $\theta$  for a single nucleon of spin  $j$  orbiting a prolate deformed nucleus. Reproduced with permission from [13].

In a deformed nucleus, the single particle orbits can have different inclinations relative to the axis of symmetry. The inclination affects the energy of the particular orbit, depending on the average distance between the orbit and the rest of the nucleus. When the orbiting nucleon remains close to the central nuclear mass, it will be more tightly bound (due to the attractive strong nuclear force) and have a lower energy than a nucleon that orbits at a higher inclination angle and spends the majority of the orbit at a greater distance from the central mass. These two orbits are shown in Figure 8.

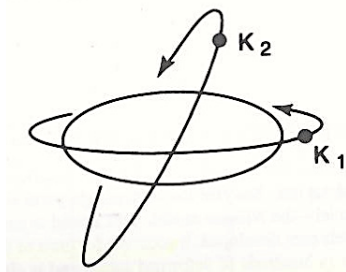


**Figure 8.** Two nucleon orbits for a prolate nucleus at different inclination angles  $\theta$ . In this figure, the orbit labeled  $K_1$  has a lower energy than the one labeled  $K_2$ . Reproduced with permission from [13].

## 2.3 Collective Models

Collective models treat the nucleus as a whole, instead of accounting for the interactions between individual nucleons. The average motion of the protons and neutrons is used to explain empirical observations.

### Liquid Drop Model.

The most familiar collective model of the nucleus is the so-called liquid drop model. The liquid drop model was initially developed by H. Bethe and C. Weizsäcker, and it shows good qualitative agreement with experiment in the case of predicting nuclear binding energies.

### Bohr-Mottelson Model.

Much like in atomic and molecular physics, in which molecular rotational and vibrational states are evident from features in visible or infrared spectra, the nucleus can exhibit collective vibration and rotation. This collective motion is the basis for the nuclear model proposed by A. Bohr and B. Mottelson in the 1950s.

The collective model of Bohr and Mottelson incorporates asymmetries in the nucleus, and so accounts for the non-spherical nature of mid-shell nuclei. In their model, in addition to rotations perpendicular to the axis of symmetry (which approximates a quantum rigid rotor) the nucleus can experience  $\beta$  or  $\gamma$  vibrations corresponding to the parameters  $\beta$  and  $\gamma$  described in Section 2.2 [11]. In a  $\beta$  vibration the nucleus extends and contracts parallel to the axis of symmetry (the football or frisbee gets longer or wider, respectively). In a  $\gamma$  vibration the nucleus extends and contracts in a direction perpendicular to the axial direction. These vibrations are illustrated in Figure 9.

The spectral features that the model predicts are most clearly evident in  $\gamma$ -ray

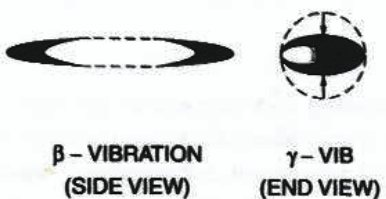


**Figure 9.**  $\beta$  and  $\gamma$  vibrational modes of deformed nuclei. A  $\beta$  vibration extends the nucleus along its principal axis, while a  $\gamma$  vibration is a periodic variation in the degree of axial asymmetry. Reproduced with permission from [13].

spectra of even-even nuclei. In these spectra, clear periodicities are evident in the  $\gamma$ -ray energies, corresponding to vibrational or rotational excitation of the nucleus. These can be organized into distinct bands, where  $\gamma$ -ray transitions between bands are generally hindered by quantum mechanical selection rules.

Application of the collective model to determine the vibrational and rotational energies of odd-odd, odd-even or even-odd nuclei requires additional approximations [11, 13]. For this purpose, combined models that incorporate both collective and microscopic approaches provide a means of describing the structure of nuclei such as  $^{186}\text{Re}$  from a theoretical standpoint.

## 2.4 Combined Models

An explanation of the structure of nuclei with an odd number of neutrons or protons requires a combination of microscopic and collective models discussed in Sections 2.2 and 2.3. Combined models are generally built on a “core plus valence nucleon” description to explain nuclear behavior [11].

### Independent Particle Approximation.

The most basic combined model is the independent particle approximation, in which the nuclear properties are assumed to arise from the motion of the unpaired valence nucleons. This is basically equivalent to the statement that the individual

nucleon-nucleon interactions of the microscopic model can be approximated by a common nuclear potential, i.e. a mean-field approach. This approximation drastically simplifies shell model calculations, since a difficult  $N$ -body problem reduces to a problem in perturbation theory. This allows the shell model to be reasonably applied to nuclei with  $N$  or  $Z$  away from the magic numbers [13].

An illustrative example of the independent particle approximation is the estimation of the ground-state spin  $J$  of a nucleus with an odd number of protons or neutrons. Since the spins of paired nucleons cancel to 0, the total spin  $J$  of a nucleus with an odd number of protons or neutrons will equal the spin  $j$  of its lone unpaired nucleon. For an odd-odd nucleus, the total spin is determined by taking the vector sum of the spins of the two unpaired nucleons [14].

The independent particle approximation can help to explain why level densities observed at low excitation energies of even-odd, odd-even or odd-odd nuclei are greater than those predicted by the shell model of the nucleus. In even-odd, odd-even or odd-odd nuclei, nucleon spins (proton, neutron, or both) are inherently unpaired. The energy required to excite the nucleus to a higher-energy state is greater when the nucleus consists of paired nuclei, as energy is required to break apart nucleon pairs. Since less energy is required to excite nuclei with unpaired nucleons, even-odd, odd-even and odd-odd nuclei are found to have higher level densities at low excitation energies [14].

## 2.5 Metastable Excited States (Isomers)

The long half lives of nuclear isomers are a direct result of selection rules that govern  $\gamma$  decay. The Weisskopf estimates are helpful for explaining the behavior of nuclear isomers. Long-lived isomers typically have spin-parity ( $J^\pi$ ) assignments that differ significantly from that of the states to which they can decay. Per the selection

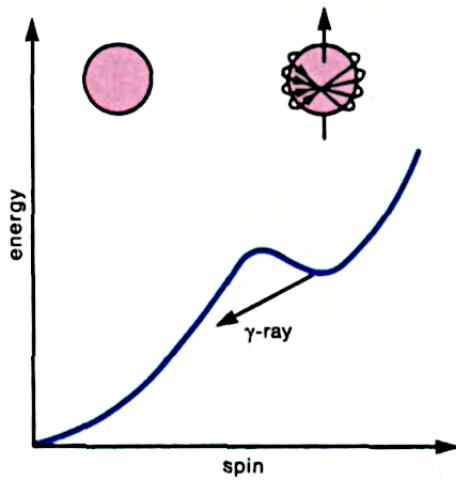
rules, a direct transition from the isomer to a lower-energy state would have a high multipole order. Thus, in a so-called spin-trap nuclear isomer, significant differences in angular momentum between the initial and final states result in very low transition rates, or long half lives [8, 12, 16]. The Weisskopf estimates also imply that low-energy transitions are inhibited.

Another factor adding to the long half lives of certain isomeric states is  $K$ -hindrance, which is an effect only observed in axially symmetric deformed nuclei, generally in the mass-180 region as shown in Figure 3. The orientation of the nuclear angular momentum  $J$  relative to the axis of symmetry, which is given by the quantum number  $K$  as described in Section 2.2, governs the ability of the nucleus to decay from an excited state to the ground state. Selection rules derived from the Nilsson model require that the multipole order  $L$  be equal to or greater than the change in  $K$  between the initial and final (ground) state. This selection rule is not strictly observed, and symmetry breaking in the model can lead to transitions in which  $L < \Delta K$ , though such transitions are hindered. Isomers in which this is found to be the case are known as  $K$ -trap isomers [12, 16].

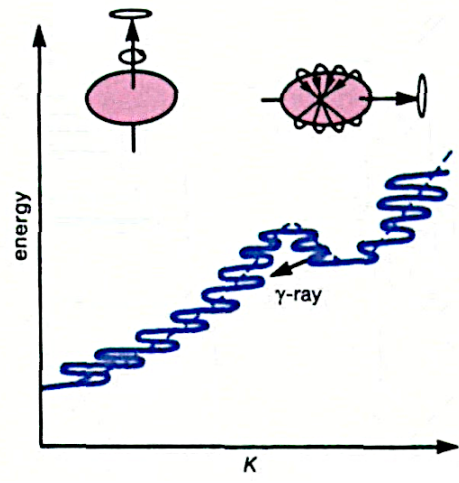
The nuclear shapes of spin-trap and  $K$ -trap isomers are illustrated in Figure 10. Per the independent particle approximation, the angular momentum arises from the motion of a small number of valence nucleons, shown orbiting the nuclei at the top of each panel. In the  $K$ -trap isomer shown in the figure, the nucleus in the isomer state is shown with its angular momentum projection 90° to that of the ground state, such that the  $\Delta K$  between the isomer and ground state is maximized.

### Population and Depletion of Isomers.

Because of the low probabilities for transition directly between the isomer state and lower-energy states, population or depletion of nuclear isomers is generally



(a) Spin-trap isomer



(b)  $K$ -trap isomer

**Figure 10.** Schematic plot of excitation energy versus angular momentum  $J$  in spin trap isomers (a) and angular momentum projection  $K$  in  $K$ -trap isomers (b). The variation in the curve shown in (b) is due to a wobbling motion of the deformed nucleus. In both cases, the excitation energy has a local minimum at the energy of the isomer state. Figure copyright 1994, IOP Publishing. Reproduced with permission from [12].

achieved by exciting the nucleus to a higher-lying intermediate states (IS) from which it can then decay to the isomer or lower-energy state, respectively. These intermediate states are more closely matched in spin to both the isomer and lower-lying state [8]. In the population of isomers by photon absorption, a photon closely matched in energy to the energy of the IS can resonantly excite the nucleus into the IS. From the IS, the nucleus can decay via  $\gamma$ -ray cascade or internal conversion to feed the isomer, or it can decay back to the initial state [17, 18]. In reverse, depletion of nuclear isomers involves excitation of the isomer to an IS from which it can decay to a lower-energy state and release the excitation energy of the isomer in the process. These two processes are illustrated in Figure 11.

If a given IS at energy  $E$  has a transition width  $\Gamma$ , then a photon of energy  $E \pm \Gamma/2$  has a high probability of resonantly exciting the nucleus into the IS. Each intermediate state that feeds the isomer thus has a cross section for resonant photon

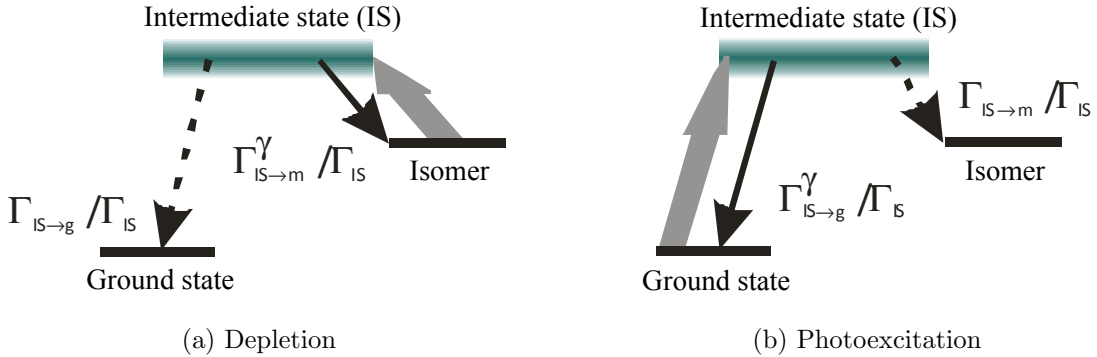


**Figure 11.** Hypothetical isomer depletion (a) and photoexcitation (b) schemes. The grey arrows identify resonant photon absorption and excitation from the initial state (isomer in (a), ground state in (b)) to the intermediate state (IS), and the dashed line is the  $\gamma$ -ray cascade to the final state (ground state in (a), isomer in (b)). Figure copyright 2013, AIP Publishing, LLC. Reproduced with permission from [18].

absorption related to its associated ground state transition width  $\Gamma$ . Since the resonances are generally very narrow compared to the energy widths in typical photon irradiation source spectra, the cross sections are typically given as integrated cross sections (ICS) in the literature [17, 19].

### Photoexcitation by Bremsstrahlung.

One method of resonantly exciting a nucleus into an isomer is through irradiation by bremsstrahlung. Bremsstrahlung photons are continuously distributed in energy up to the endpoint energy of the accelerated electrons used to create them. If  $E$  is photon energy,  $\frac{d\Phi}{dE}$  represents the spectral flux density of the bremsstrahlung source, and the number  $N_f$  of nuclei in a particular sample excited into the isomer from  $N_i$  initial nuclei is

$$N_f = N_i \sum_j \text{ICS}_{fj} \frac{d\Phi}{dE}. \quad (7)$$

Here the sum is over all intermediate states that feed the isomer, identified by index  $j$ . The term  $\text{ICS}_{fj}$  is the integrated cross section for population of the isomer via

the  $j^{th}$  IS [20].

This energy- and angle-integrated cross section can be evaluated directly using data available in nuclear databases such as the ENSDF. Dracoulis, et al. identifies the integrated cross section for an isolated  $(\gamma, \gamma')$  resonance with photon wavelength  $\lambda$  from an initial state with angular momentum  $J_i$  to an intermediate state with angular momentum  $J_j$  as

$$\text{ICS}_{fj} = \int_E \sigma(E) dE = \frac{\lambda^2}{4} g \frac{\Gamma_{j \rightarrow i} \Gamma_{i \rightarrow f}}{\Gamma_j}, \quad (8)$$

with a statistical factor  $g$  given by

$$g = \frac{2J_i + 1}{2J_j + 1}. \quad (9)$$

The decay width of the intermediate state in Equation 8 is  $\Gamma_j$ , while  $\Gamma_{j \rightarrow i}$  is the decay width of all paths that reach the isomer state and  $\Gamma_{i \rightarrow f}$  is the width for decay from the IS directly to the final state [21]. In the case of photoexcitation, the initial state is the ground state of the nucleus while the final state is that of the isomer. The indices are reversed in the case of isomer depletion. The cross sections for photoexcitation and depletion are different as a result of the differing statistical factors and the fact that a given state cannot typically be an IS for both processes. Unfortunately this formula has limited utility in practice, as the natural decay width  $\Gamma$  depends on the level lifetime  $\tau$  according to  $\Gamma = \hbar/\tau$ , and these level lifetimes are unknown for many levels in the ENSDF. Instead, integrated cross sections can be deduced by direct measurement of inelastic photon excitation, the results of which are sometimes published [17, 20].

## 2.6 Neutron-Induced Excitations

In the experiment described in this work,  $(n, xn\gamma)$  reactions with  $x \geq 1$  were used to study the excited states of rhenium nuclei. In these reactions, an incident high-energy neutron imparts energy to the target nucleus through the formation of a compound nucleus. The excitation energy, which includes both the kinetic energy and the binding energy of the neutron, is distributed among the nucleons according to equipartition of energy. When a nucleon in the compound nucleus achieves enough energy to tunnel through the potential barrier of the nucleus, it is emitted from the nucleus. In the case where the emitted particle is a neutron, the height of the potential barrier is equal to the neutron separation energy and this process is known as neutron evaporation [22]. For  $(n, xn\gamma)$  reactions with  $x \geq 1$ , the excitation energy of the compound nucleus is sufficient to overcome the separation energy of  $x$  neutrons in the nucleus, and these neutrons escape from the nucleus as a result. After neutron emission, the residual nucleus is generally left in an excited state, and it decays via  $\gamma$ -ray cascade or internal conversion to the ground state or to an isomer.

Internal conversion is a process that competes with  $\gamma$  decay, in which an electron from an inner atomic shell is ejected from the atom as a means of reducing the excitation energy of the nucleus. Following the emission of the conversion electron from the inner atomic orbital, outer electrons will fill the vacancy, emitting a cascade of X-rays or Auger electrons in the process [14]. These characteristic X-rays appear prominently in most  $\gamma$ -ray spectra. The internal conversion coefficient  $\alpha$  is defined such that the probability a given excited state will decay via internal conversion instead of  $\gamma$  decay is  $\alpha/(1 + \alpha)$ . Conversion coefficients are included in the calculation of partial  $\gamma$ -ray cross sections from measured  $\gamma$ -ray yields for the nuclear transitions of interest in this experiment. These conversion coefficients are

generally published in the Table of Isotopes [2], or they can be computed using the BrIcc conversion coefficient calculator [23].

The two primary reactions reflected in the data taken with the GEANIE detector array were  $^{187}\text{Re}(n, n'\gamma)^{187}\text{Re}$  and  $^{187}\text{Re}(n, 2n\gamma)^{186}\text{Re}$ . Although  $(n, xn\gamma)$  reactions with  $x \geq 3$  also occurred in the target, because of the small cross sections for these reactions compared to those of the  $x = 1$  and  $x = 2$  reactions there were less data available to analyze. Furthermore, the focus of this research in particular was on the structure of  $^{186}\text{Re}$  revealed through the  $^{187}\text{Re}(n, 2n\gamma)^{186}\text{Re}$  reaction, so analysis of the data from other reactions was a lesser priority.

### **Reaction Energetics and Cross Sections.**

Neutron-induced reactions have thresholds governed by the binding energy of the compound nucleus and the neutron separation energy of the target nucleus. As a rough approximation, the neutron separation energy of the target nucleus represents a threshold below which  $(n, 2n\gamma)$  reactions are energetically forbidden. In this approximation, the  $^{187}\text{Re}$  nucleus must be excited to an energy at least as great as the neutron separation energy  $S_n$  of the  $^{187}\text{Re}$  nucleus to cause the reaction to occur and create  $^{186}\text{Re}$ . The neutron separation energy is given by K. Krane for an arbitrary nucleus  ${}_Z^A\text{X}_N$  as

$$S_n = [m({}_{Z}^{A-1}\text{X}_{N-1}) - m({}_{Z}^A\text{X}_N) + m_n] c^2. \quad (10)$$

For  $^{187}\text{Re}$  this separation energy is equal to 8.3 MeV [14].

The probabilities of decay of the compound nucleus via different reaction channels lead to cross sections for the various reactions. The cross sections for the  $^{187}\text{Re}(n, xn)^{188-x}\text{Re}$  reactions ( $1 \leq x \leq 3$ ) are plotted in Figure 12 using data obtained from the Evaluated Nuclear Data File (ENDF). Due to the lack of

experimental data for neutron-induced reactions in  $^{187}\text{Re}$ , the cross section data adopted for the most recent ENDF database, ENDF-VII.1, consists of values calculated by the TALYS nuclear reaction modeling code (further described in Section 5.3 of this document). These calculated cross sections are described as a good fit to the available experimental data [24].

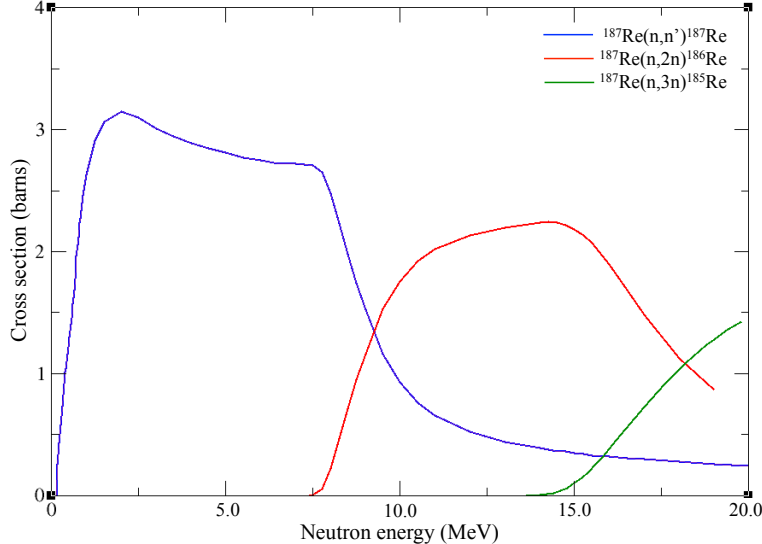


**Figure 12.** Cross sections for  $(n, n')$ ,  $(n, 2n)$  and  $(n, 3n)$  reactions in  $^{187}\text{Re}$ , plotted against neutron energy  $E_n$ . For  $E_n > 1.0$  MeV the cross section for radiative capture  $(n, \gamma)$  is negligible compared to the reactions shown. Data for this plot were obtained from the ENDF [24, 25].

As anticipated, above the  $^{187}\text{Re}$  neutron separation energy of 8.3 MeV, the cross section for the  $^{187}\text{Re}(n, n')^{187}\text{Re}$  reaction decreases as the  $(n, 2n)$  reaction becomes possible. Similarly, the cross section for the  $^{187}\text{Re}(n, 2n)^{186}\text{Re}$  reaction decreases and that of the  $^{187}\text{Re}(n, 3n)^{185}\text{Re}$  reaction increases above approximately  $2 \times 8.3$  MeV = 16.6 MeV. This allows selection thresholds, or cuts, to be defined at neutron energies of  $\sim 10$  MeV and  $\sim 20$  MeV to separate the reaction products by reaction channel during the experimental data analysis.

## 2.7 Literature Review

The ENSDF database identifies a total of 24 references for nuclear data concerning  $^{186}\text{Re}$ . Of these 24 references, two are compiled nuclear data sheets, and two are articles written in German. Of the remaining original articles, two describe the level scheme, and the remainder are concerned with other nuclear data such as the half life or quadrupole moments [7, 15]. In addition, since the most recent evaluation in 2002, two other references have been published that describe the level scheme of  $^{186}\text{Re}$  [26, 27].

### Nuclear Structure and Isomer Discovery.

The  $^{186}\text{Re}$  nucleus consists of 75 protons and 111 neutrons. By nature of the fact that it is an odd-odd nucleus, its level scheme is complex, and it has a particularly high level density at low energies. Regularly spaced rotational and vibrational bands predicted by collective models that are evident in even-even nuclei are not immediately apparent in the  $^{186}\text{Re}$  level scheme. The deformed potential (Nilsson) model discussed in Section 2.2 is required to determine the intrinsic energy levels in  $^{186}\text{Re}$ , a prolate nucleus.

An initial analysis of the nuclear structure of  $^{186}\text{Re}$  was performed by Lanier and others in 1969 [15]. This was followed by the discovery of a long-lived isomer at 149(7) keV in 1972 by Seegmiller, Lindner, and Meyer [7]. This isomer, which has spin-parity  $J^\pi = 8^+$ , was observed to decay via  $\gamma$ -ray emission to the ground state with a half life of  $2 \times 10^5$  years. An extract from the level scheme for  $^{186}\text{Re}$  is shown in Figure 13.

Evident in the figure is the  $\sim 50$  keV transition by which the  $\sim 150$  keV isomer decays to the  $J^\pi = 3^-$  state at 99.3 keV. From the 99.3 keV state, the nucleus can de-excite by direct  $\gamma$ -decay to the ground state or by cascade involving 40.3 keV and

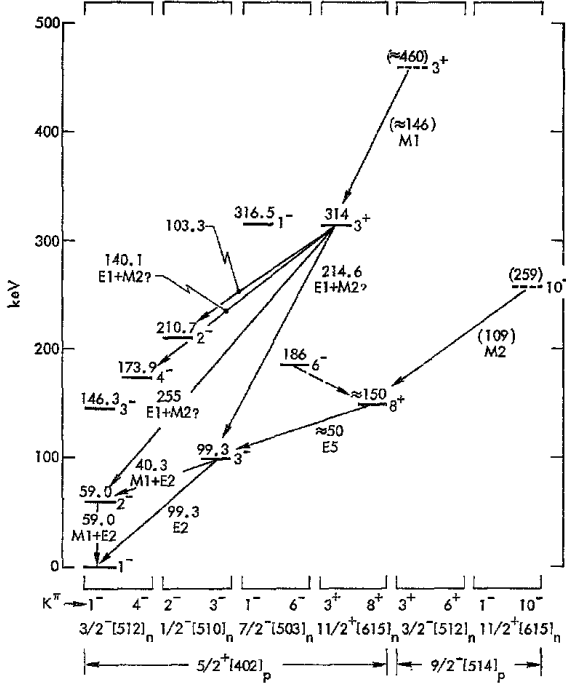


**Figure 13.** Selected intrinsic levels in  $^{186}\text{Re}$  showing the single-nucleon quantum numbers in the Nilsson convention  $K^\pi [Nn_z\Lambda]$  below the horizontal axis. The spherical state spin-parity  $J^\pi$  from which each state arises is identified next to the the respective level in the diagram. Dashed lines and parentheses identify tentative assignments. Figure copyright 1972 Elsevier B.V. Reproduced with permission from [7].

59 keV  $\gamma$ -rays. Transitions from the  $J^\pi = 8^+$  isomer to lower spin states are inhibited by the spin differences between these states.

A recent work by Wheldon and others utilized a 21 MeV proton beam to excite  $^{186}\text{Re}$  nuclei via the transfer reaction  $^{187}\text{Re}(p, d)^{186}\text{Re}$ , and identified 30 levels above 400 keV that had not previously been observed [26]. The new levels discovered during the experiment were compared against theoretical models to propose Nilsson configurations for several levels, though others are identified with no proposed spin-parity assignment. The data from this experiment are included in the XUNDL.

### Recent Analysis of an Isomer Feeding Mechanism.

A 2014 AFIT thesis by A. Lerch examined spectra from an experiment involving  $^{185}\text{Re}(n, \gamma)^{186}\text{Re}$  reactions performed at the Budapest Research Reactor (BRR). The

results included discovery of 12 levels and 54 transitions not previously identified, but a transition feeding the 149(7) keV isomer level was not among these [27]. The work proposed that a possible mechanism is one in which the isomer is fed by an *E2* transition from the 186 keV level to the 149 keV isomer level, but no experimental or modeled data were available to support this hypothesis.

### III. Experiment

#### 3.1 Experimental Facilities

The experiment took place at the Los Alamos Neutron Science Center (LANSCE) Weapons Neutron Research (WNR) facility from 10 November to 9 December 2014, utilizing the GErmanium Array for Neutron Induced Excitations (GEANIE) detector array.

##### LANSCE/WNR.

The LANSCE accelerator is a proton linear accelerator (LINAC) capable of producing protons in two distinct beams at energies up to 800 MeV. The accelerator produces pulses of protons at a macropulse repetition rate of 60 or 120 Hz and average currents of 0.5 to 4  $\mu$ A. The beam is split at locations along the beam line and pulses are delivered to various experiments at LANSCE. Of the 60 or 120 Hz produced by the accelerator facility, 40 or 100 Hz, respectively, is generally the macropulse rate as it is delivered to the GEANIE target. The macropulses, which are each 625  $\mu$ s in duration, comprise numerous sub-nanosecond micropulses spaced 1.8  $\mu$ s apart.

For experiments at the WNR, the 800 MeV protons are directed at one of two tungsten targets to produce sources of spallation neutrons for the various flight paths, illustrated in Figure 14. Each target is located under a large mound of concrete that provides necessary shielding.

Flight paths originating from target 4 receive an unmoderated flux of neutrons with energies ranging from 100 keV to nearly 600 MeV, depending on the angle between the flight path and the proton beam (Figure 15).

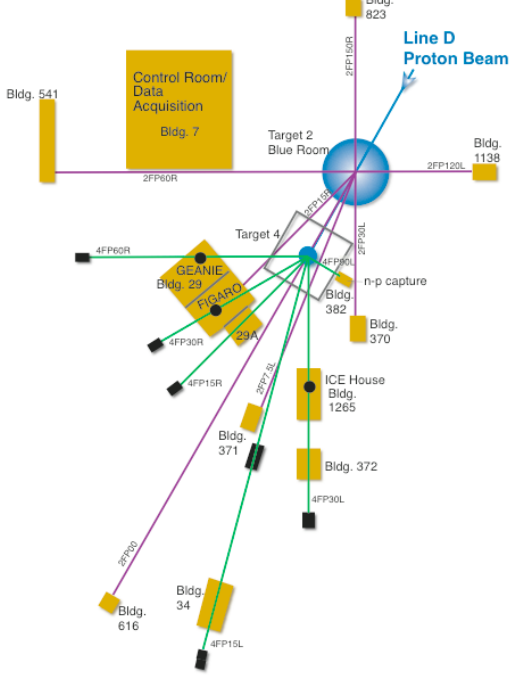


**Figure 14.** The LANSCE/WNR facility consists of two spallation targets and associated flight path experiments. GEANIE uses neutrons produced at Target 4, while the Blue Room experiments at Target 2 involve exposing targets directly to the 800 MeV proton beam. Diagram authored by an employee or employees of Los Alamos National Security, LLC (LANS), operator of the Los Alamos National Laboratory under Contract No. DE-AC52-06NA25396 with the U.S. Department of Energy. Reproduced with permission from [28].

## GEANIE.

The GEANIE spectrometer is an array of high-purity germanium (HPGe) detectors located at  $60^\circ$  right off the proton beam line. The array is used for  $\gamma$ -ray spectroscopy experiments that include nuclear structure investigations and cross section measurements for various nuclear technology and national security applications [28]. A schematic of the neutron beam tube, fission chamber and GEANIE detector array is shown in Figure 16.

Neutron energies of 0.6 to  $\sim 200$  MeV are available at the target in GEANIE experiments [30, 31]. The neutron flux at the target is measured using a fission chamber positioned at the terminus of the neutron beam tube, 18.48 m from the

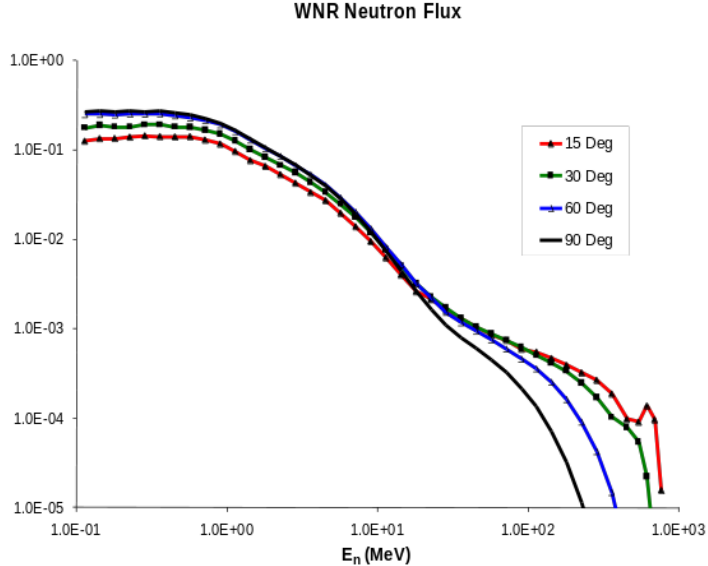


**Figure 15.** Neutron flux spectra (log-log scale) for target number 4 at LANSCE/WNR, a tungsten spallation target. Neutrons are produced with energies up to 800 MeV. The units of the vertical axis are arbitrary flux units defined such that each flux distribution is normalized. Diagram authored by an employee or employees of the Los Alamos National Security, LLC (LANS), operator of Los Alamos National Laboratory under Contract No. DE-AC52-06NA25396 with the U.S. Department of Energy. Reproduced with permission from [28].

spallation target [32]. The fission chamber consists of an ionization chamber that incorporates iron foils impregnated with  $^{235}\text{U}$  and  $^{238}\text{U}$ , so that the known fission cross sections of these isotopes can be used to calculate the neutron flux from the counts of fission events in the ionization chamber [33]. The size of the neutron beam arriving at the target is adjusted using an iron collimator, prior to the beam transiting the fission chamber. For this experiment, the beam was trimmed to a diameter of  $1/2''$  (1.25 cm).

The detector array, shown in Figure 17, is positioned 20.34 m from the spallation target and includes a mix of planar and coaxial geometry detectors to optimize resolution and efficiency across a wide range of  $\gamma$ -ray energies. Coaxial HPGe detectors have a greater efficiency at  $\gamma$ -ray energies of  $\sim 400$  keV and higher, while planar detectors have a better low-energy efficiency. The gain on the two detector

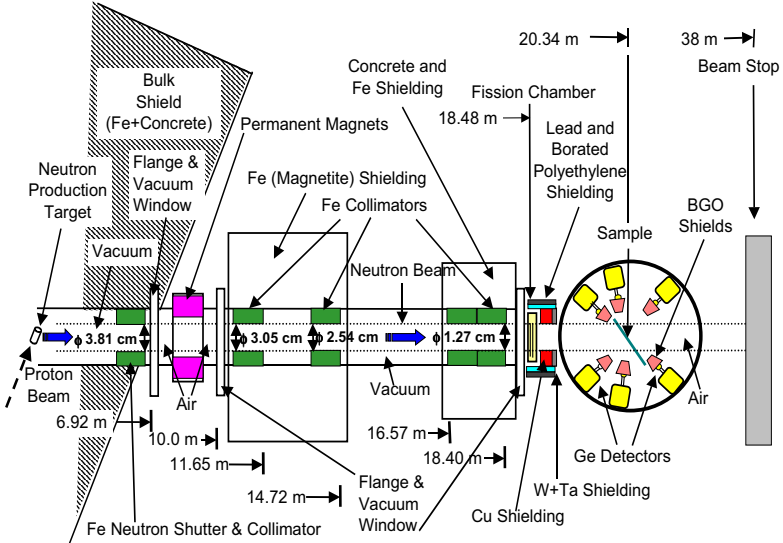


**Figure 16.** Schematic diagram of the  $60^\circ$  right flight path from target 4 at LANSCE/WNR and the GEANIE detector array. Diagram authored by an employee or employees of Los Alamos National Security, LLC (LANS), operator of the Los Alamos National Laboratory under Contract No. DE-AC52-06NA25396 with the U.S. Department of Energy. Reproduced with permission from [29].

types is set in the hardware to reflect this difference. The planar gain is set to achieve full-scale (8192 channel) deflection at  $E_\gamma = 1.0$  MeV, while the coaxial gain is set such that full-scale deflection occurs at  $E_\gamma = 4.0$  MeV. Because of neutron damage to the semiconductor crystals, some detectors failed to produce usable spectra, which impacted the quantity of  $\gamma - \gamma$  coincidence data produced.



**Figure 17.** The GEANIE detector array at LANSCE/WNR, with the enriched  $^{187}\text{Re}$  sample mounted in the center of the array. The beam originates from the far right of the array in the photograph. This picture was taken with the detector array opened, so approximately 2/3 of the 18 installed detectors are visible.

The detector array has mounts for 26 HPGe detectors, which provide nearly  $4\pi$  coverage of the target. For the rhenium experiment, these detectors were mounted in the array according to the diagram shown in Figure 18. Two positions in the 20 circumferential locations were left vacant in this experiment due to detector non-availability. Of the 18 detectors installed during this experiment, all were Compton-suppressed using bismuth germanium oxide (BGO) detectors. The 6 overhead detector mounts, which can accommodate unsuppressed HPGe detectors, were also left empty for the rhenium experiment due to detector non-availability. For this particular experiment, the detector array consisted of 18 serviceable detectors, a mix of 8 planar and 10 coaxial detectors.

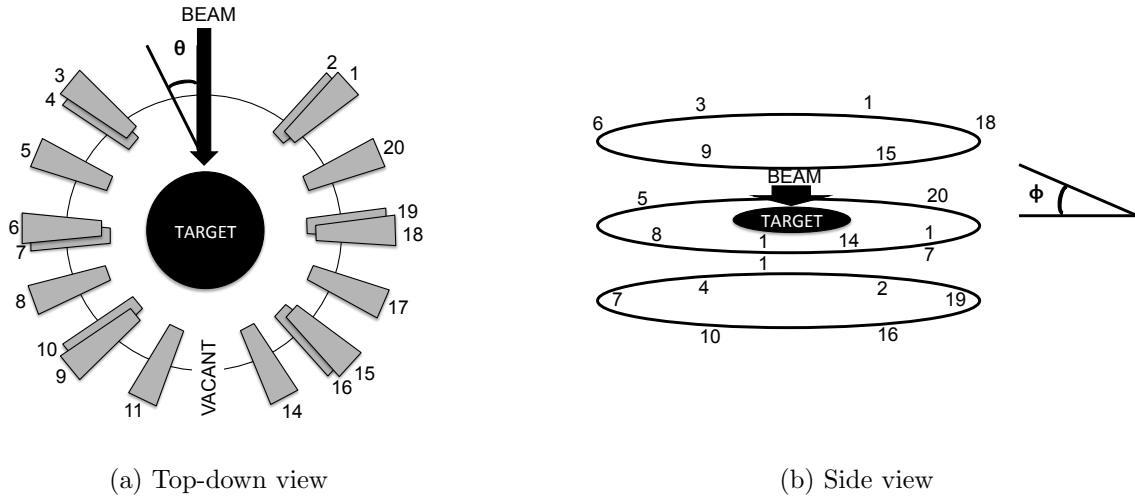


Figure 18. Diagram of the HPGe detector locations in the GEANIE array (not to scale), viewing from (a) top down perspective and (b) side perspective, with the neutron beam coming out of the page. The diagrams identify the 18 detectors that were installed and functional in the array at the time of the experiment. Letters identifying the detector are referenced in Table 1 with the azimuthal angle  $\theta$  and angle of elevation  $\phi$ .

The polar and azimuthal detector locations relative to the target are listed in Table 1 [29]. Remarks in the table identify problems with certain detectors encountered during the experiment and data analysis, described further in Chapter IV.

**Table 1.** GEANIE detector positions by azimuthal angle  $\theta$  and angle of elevation  $\phi$  relative to beam axis. The mounts for detectors 12, 13, and 21 – 26 were empty during this experiment.

Detector	Type	$\phi$	$\theta$	Distance	Remarks
1	Planar	29.0°	-152.8°	14.415 cm	
2	Planar	-29.0°	-154.0°	14.442 cm	
3	Planar	29.0°	1.0°	14.379 cm	
4	Coaxial	-29.0°	1.2°	14.773 cm	
5	Planar	0.0°	26.5°	14.308 cm	Double peaks in TDC spectrum
6	Coaxial	29.0°	53.0°	14.455 cm	
7	Coaxial	-29.0°	53.5°	14.435 cm	
8	Planar	0.0°	78.5°	14.917 cm	
9	Planar	29.0°	102.0°	14.237 cm	
10	Planar	-29.0°	102.5°	14.288 cm	
11	Coaxial	0.0°	129.5°	14.237 cm	No counts after run 9773
14	Coaxial	0.0°	-25.2°	14.392 cm	Double peaks in TDC spectrum
15	Coaxial	29.0°	-51.1°	14.392 cm	Double peaks in TDC spectrum
16	Coaxial	-29.0°	-51.0°	13.846 cm	Unstable ADC gain
17	Coaxial	0.0°	-76.9°	14.442 cm	
18	Coaxial	29.0°	-101.7°	14.176 cm	
19	Coaxial	-29.0°	-102.0°	14.308 cm	
20	Planar	0.0°	-128.0°	14.161 cm	

### Compton Suppression.

The response function of HPGe detectors, like all  $\gamma$ -ray detectors of finite size, includes a continuum of partial energies deposited in the detector corresponding to the energies of Compton electrons scattered by the incident  $\gamma$ -ray. The Compton continuum extends up to energies of

$$E_{e^-} = \frac{2E_\gamma^2}{2E_\gamma + m_e c^2}, \quad (11)$$

where  $E_\gamma$  is the energy of the  $\gamma$ -ray,  $m_e$  is the mass of the electron, and  $c$  is the speed of light. Equation 11 identifies the maximum energy attainable by a Compton electron, when the scattering angle is  $\theta = \pi$  [14]. In  $\gamma$ -ray spectroscopy, the presence of the Compton continua from higher energy  $\gamma$ -rays represents a source of background that might obscure the full energy photopeaks from lower energy  $\gamma$ -rays.

A Compton suppression system was designed to alleviate this problem. In the design used in the GEANIE detectors, a bismuth germanium oxide (BGO) detector provides a shield surrounding each HPGe detector. BGO detectors are selected for this role because of their high relative detection efficiency, due to the presence of high- $Z$  bismuth in the detector crystals. If a Compton-scattered photon is measured in the BGO detector at the same time that a Compton electron is measured in the HPGe detector, then the signal is rejected. This anticoincidence setting ensures that the only signals sent from the suppressed HPGe detectors to the ADCs are full photopeaks.

### 3.2 Target Sample Preparation

Two targets of approximately 1 gram each were used in this experiment, a rhenium sample enriched in  $^{187}\text{Re}$  and a sample of natural rhenium. Both were ordered by Ecopulse, Inc. under a contract maintained by the Army Research Laboratory (ARL). The rhenium metal powder samples were hot vacuum pressed at Oak Ridge National Laboratory (ORNL) and sent directly to LANSCE in October and November, 2014.

#### **Enriched $^{187}\text{Re}$ Sample.**

The enriched rhenium sample was purchased from ORNL, where it was isotopically enriched to 99.52%  $^{187}\text{Re}$ . The encapsulated sample consisted of

981.7 mg rhenium metal powder.

### *nat* Re Sample.

A natural rhenium (37.4%  $^{185}\text{Re}$  and 62.6%  $^{187}\text{Re}$ ) sample was used in the last day of the experiment and consisted of 1036.2 mg of metal powder. This sample was purchased from Alfa Aesar and shipped to ORNL for encapsulation.

### Target Holders.

Polycarbonate target holders were 3-D printed in two pieces at ARL, as shown in Figure 19. These two pieces were held together by setscrew, and contained the vacuum-pressed metal pill samples after they were fashioned.

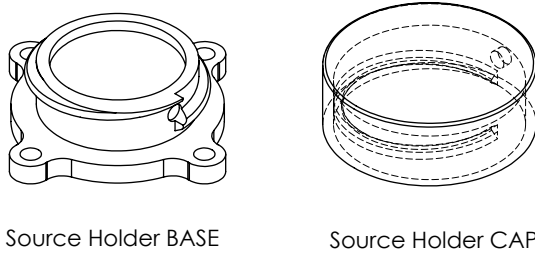


**Figure 19.** Schematic of the 3D-printed holder used to contain the pills of pressed rhenium metal powder during irradiation.

The target holder was made to eliminate the possibility of leakage of the rhenium powder during the experiment, as trace amounts of radioactive  $^{186}\text{Re}$  would be created by  $(n, 2n)$  reactions. However, concerns of leakage from the encapsulation led to special safety procedures mandated by Radiation Control Technicians (RCTs) at LANL, in which the sample was required to be tested for the presence of the  $\beta$ -emitting isotope  $^{186}\text{Re}$  each time the target sample was removed from the detector array.

### 3.3 Experiment Summary

The 21 days of beam time originally requested for the experiment was approved in two parts: the first part from 10 – 23 November 2014 and the remainder from 4 – 8 December 2014. Due to the timing of other experiments, beam was available from 3 – 9 December during the second window. During the approved beam time windows, two related experiments were scheduled involving the GEANIE detector array. The first involved the rhenium sample enriched in  $^{187}\text{Re}$  and the other involved the natural rhenium sample.

#### **Enriched $^{187}\text{Re}$ Target.**

Using the enriched  $^{187}\text{Re}$  target,  $\gamma$ -ray spectra from the  $^{187}\text{Re}(n, n'\gamma)^{187}\text{Re}$  and  $^{187}\text{Re}(n, 2n\gamma)^{186}\text{Re}$  reactions were obtained over 20 days, encompassing the 10–23 November window and the first 6 days of the 3–9 December window. The experiment was initially planned anticipating a 100 Hz macropulse repetition rate produced by the LANSCE accelerator, but beam maintenance issues led to a lower repetition rate of 40 Hz and an average proton current of approximately 1200 nA from 10–23 November. Additionally, a bad filament in the accelerator led to an unplanned 28-hour shutdown from 17–18 November. As a result of the lower current and the unplanned outage, the decision was made to extend the experiment involving the enriched target to 16 days from the 8 days originally planned.

During the planned 24 November–2 December shutdown, accelerator maintenance personnel increased the macropulse repetition rate to 100 Hz, and the experiment resumed on 3 December using the enriched target. From 3 – 9 December, the accelerator operated continuously at 100 Hz and an average proton beam current of  $\sim 3500$  nA.

## **Normalization Runs with $^{56}\text{Fe}$ .**

From 6 – 8 December, the enriched rhenium sample was sandwiched between two 0.127-mm thick  $^{nat}\text{Fe}$  foils and irradiation continued. The data obtained from these runs allows measurement of the  $\gamma$ -ray yield for the 846.8 keV transition in  $^{56}\text{Fe}$  from the  $^{56}\text{Fe}(n, n'\gamma)^{56}\text{Fe}$  reaction, relative to the  $\gamma$ -ray yields from neutron-induced reactions in rhenium. The well-known partial  $\gamma$ -ray cross section for the 846.8 keV transition in  $^{56}\text{Fe}$  is used to normalize the partial  $\gamma$ -ray cross sections generated for the rhenium isotopes, so that the rhenium cross sections can be compared with those produced by theoretical models.

## **$^{nat}\text{Re}$ Target.**

Using the sample of  $^{nat}\text{Re}$ ,  $\gamma$ -ray spectra from  $^{185}\text{Re}(n, n'\gamma)^{185}\text{Re}$  and  $^{185}\text{Re}(n, 2n\gamma)^{184}\text{Re}$  reactions were obtained in addition to the reactions involving  $^{187}\text{Re}$  over a period of 24 hours from 8 – 9 December. The intent of irradiating the natural rhenium target was to generate  $\gamma$ -ray excitation functions from the  $^{185}\text{Re}(n, 2n\gamma)^{184}\text{Re}$  channel for comparison with the excitation functions obtained from similar transitions in  $^{187}\text{Re}(n, 2n\gamma)^{186}\text{Re}$ , which will be described in more detail in Section 5.4.

## **Source Data.**

When beam operations were stopped, calibration sources were placed in the detector array for the purpose of obtaining spectra for energy and efficiency calibration of the detectors. A total of 9 calibration sources were used to cover a wide range of  $\gamma$ -ray energies:  $^{152}\text{Eu}$ ,  $^{57}\text{Co}$ ,  $^{133}\text{Ba}$ ,  $^{60}\text{Co}$ ,  $^{22}\text{Na}$ ,  $^{109}\text{Cd}$ ,  $^{137}\text{Cs}$ ,  $^{54}\text{Mn}$  and  $^{241}\text{Am}$ . Data were collected in 20-minute runs for each of these sources during the unscheduled stoppage on 17 November. Additional source data using the  $^{152}\text{Eu}$  and

$^{241}\text{Am}$  sources were also collected during the scheduled 24 November – 3 December shutdown.

The data from these sources, with the  $^{152}\text{Eu}$  source as the primary reference for energy calibration, were analyzed separately to produce energy and efficiency calibration files for use in the RadWare programs `gf3` and `escl8r`, described in further detail in Chapter IV.

### **Detector Performance.**

During the experiment, 14 of the 18 installed HPGe detectors (7 planar and 7 coaxial) produced usable spectra that were included in the data analysis. The remaining 4 detectors developed problems that prevented the inclusion of the spectra they produced in the final data set. Those issues are identified in the remarks column of Table 1, and the reasons for their non-inclusion are as follows:

- One of the installed planar detectors (5) and 2 coaxial detectors (14, 15) were identified as producing time spectra with anomalous double peaks. This effect prohibits the correlation of neutron energy  $E_n$  to the TDC channel, so these 3 detectors were eliminated from the set during analysis of the data.
- One coaxial detector (16) had a highly unstable gain that caused significant problems during gain matching, so it was eliminated from the final detector set.

Of the remaining detectors, one coaxial detector (11) ceased producing counts altogether 1 week after the experiment began. Based on this detector's location opposite the neutron source it is likely that neutron damage resulted in the detector's early failure. Prior to the failure, however, the detector produced usable spectra which were included in the final data set.

There were 11 single-channel wide lines in ADCs 1-6, which ultimately included 3 planar detectors and 2 coaxial detectors, that were attributed to the hardware, as all these detectors were connected to the same data bus. These spurious lines were noted for reference during the data analysis to remove the possibility of mis-identifying them as  $\gamma$ -ray peaks.

During the 3 – 8 December runs, Compton suppression was lost to all the detectors in the array for a period of 3 days. The problem was eventually traced to a tripped power supply, which affected the entire bus from which the BGO suppression shields received their power. The experiment was completed by the time the problem was discovered, so the  $\gamma$ -ray spectra obtained from the  $^{nat}\text{Re}$  sample included a Compton background not present in the earlier runs.

## IV. Results and Analysis

The experiment was unique in two ways: it was the first reported experiment to study  $^{187}\text{Re}$  with an  $(n, n')$  reaction, and the first to study  $^{186}\text{Re}$  with a  $(n, 2n)$  reaction. As a result, it was expected that the experiment would result in the discovery of new  $\gamma$ -ray transitions in both isotopes. The initial goals of data analysis following the experiment were to identify  $\gamma$ -ray peaks in the ADC spectra produced by the HPGe detectors attributable to new transitions in  $^{186}\text{Re}$  and  $^{187}\text{Re}$ .

### 4.1 Data Acquisition and Online Analysis

Data acquired by GEANIE were first analyzed online, while the experiment was running, prior to being saved for offline data analysis. The steps involved in this process are shown schematically in Figure 20.

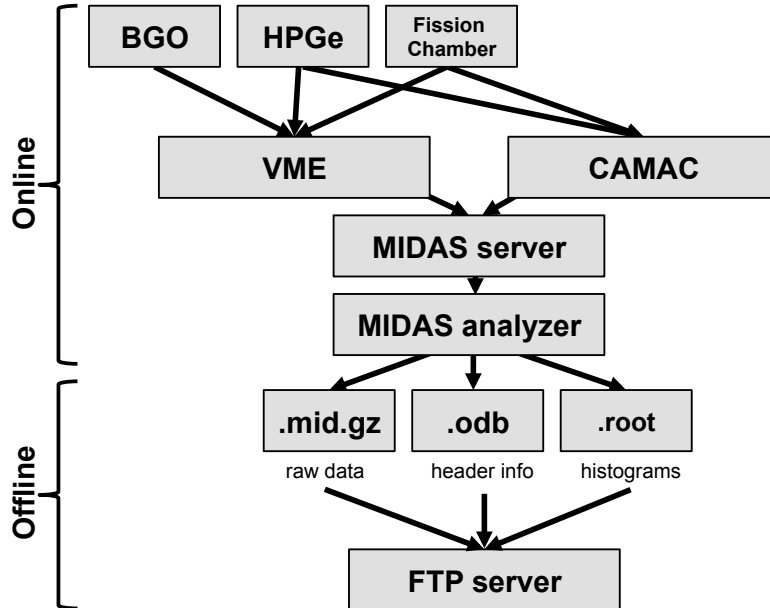


Figure 20. Flow chart showing the process of data acquisition, storage and transfer. The necessary files for offline data analysis consisted of ROOT histograms (.root) and MIDAS raw data (.mid.gz) and online database (.odb) information.

## **Data Acquisition Framework.**

In the online phase of the analysis,  $\gamma$ -ray energy and neutron time-of-flight (TOF) data were acquired by analog-to-digital converters (ADCs) and time-to-digital converters (TDCs). The ADC and TDC signals were sent to Versa Module Europa (VME) and Computer Automated Measurement and Control (CAMAC) servers that interfaced with a Linux workstation operating as a Data Acquisition (DAQ) server. The VME server handled data sent to the VME bus, which included ADC and TDC signals from each of the HPGe detectors in the GEANIE array and the fission chambers. Signals from scalers, which recorded clock timing data and the total ADC counts over each 10-second period of runtime (necessary for calculating detector deadtime), were sent through the CAMAC server.

All experiments at LANSCE/WNR, including GEANIE, use the Maximum Integrated Data Acquisition System (MIDAS) software package as the DAQ framework to interface with the VME and CAMAC hardware. MIDAS was developed at the Paul Scherrer Institute, Switzerland for particle physics experiments, and is open-source software.

## **MIDAS Analyzer.**

Data from each  $\gamma$ -ray event were compiled on the MIDAS server using an analyzer program written at LANSCE, which performed online analysis of the VME and CAMAC signals to produce event data that makes up each run. After each run was completed, the MIDAS analyzer packaged and compressed the run files, and data from each run were saved to disk. The files produced at this point included the raw data from each  $\gamma$ -ray event in the run, saved in a proprietary MIDAS format and compressed with the file extension `.mid.gz`, histograms that display the various ADC and TDC spectra in a ROOT format, and an online database (`.odb`) file

containing various header information about the run for use by the MIDAS analyzer program. The largest of these files from each run was generally the `.mid.gz` file, which ranged in size for each run from several hundred megabytes to over a gigabyte, depending on the run duration.

The `.mid.gz`, `.odb` and `.root` files were saved locally to disk on the MIDAS server automatically following each run, and the next run started automatically according to the preset run times. The run times were adjusted throughout the experiment to minimize data loss while also limiting the total number of data files created. The online MIDAS analyzer experienced frequent crashes, particularly when the data rate was high, as was the case during beam operations at the higher 100 Hz macropulse repetition rate. Setting the run time to a smaller value insured against data loss when the analyzer crashed, as the program would stop and restart itself automatically at the prescribed time and clear the buffer in the process. In general, run times varied between 20 minutes and 6 hours.

### **Data Transfer and Storage.**

Periodically throughout the experiment, the files were uploaded to the LANL public FTP server, from which they were downloaded to an external hard drive. At the end of the experiment, the total data accumulated on the hard drive was 62.4 GB in size, which included data from 441 runs.

## **4.2 Offline Data Analysis Methodology**

The MIDAS event files were converted into  $\gamma$ -ray energy ( $E_\gamma$ ) versus neutron energy ( $E_n$ ) matrices during the offline phase of data analysis. These  $E_\gamma$  vs.  $E_n$  matrices were then parsed into  $\gamma$ -ray spectra gated on specific neutron energy ranges.

## **Software Alternatives for Data Analysis.**

In order to convert MIDAS event files to viewable data structures, they had to be converted to be viewed by an appropriate offline analysis package. Two alternatives were available for this analysis: ROOT and TScan. With TScan, the  $\gamma$ -ray spectra are analyzed using programs included in the RadWare software package.

### **ROOT.**

ROOT is an open-source collection of C++ libraries developed and maintained at CERN. The well-documented libraries include statistics and peak fitting tools that allow users to analyze spectra directly. It is considered a standard for data analysis in many nuclear and particle physics experimental facilities. The MIDAS analyzer is capable of producing ROOT trees and histograms in an offline mode, so ROOT can be used to perform spectral analysis of GEANIE data [34, 35]. Of interest in this experiment, however, was the generation of  $\gamma - \gamma$  coincidence matrices, for which there were no tools built in ROOT.

### **TScan.**

The TScan software package was written by H. Jin at Rutgers University to perform tape scanning and manipulate matrices [36]. It has been used for data analysis in numerous GEANIE experiments [1, 29, 32, 37, 38, 39]. Though TScan is no longer maintained, it can still be compiled and run on a 32-bit Linux operating system. Numerous subroutines developed specifically for analyzing data from GEANIE experiments have been written by W. Younes of Lawrence Livermore National Laboratory, including a tool for generating coincidence matrices [40]. As a result, TScan was adopted for data analysis in this experiment despite its legacy status.

## **RadWare.**

RadWare is an open-source software package for analyzing one-dimensional (singles)  $\gamma$ -ray spectra and constructing nuclear level schemes from  $\gamma - \gamma$  coincidence data, among other functions [41]. It was developed by D. Radford, currently of ORNL, and it is used widely throughout the nuclear physics community. The spectra and coincidence matrices produced by TScan and associated subroutines were analyzed using the `gf3` and `escl8r` programs included with the current RadWare version rw05.

## **Data Analysis Using TScan and RadWare.**

After the experiment was completed and the data files downloaded from the FTP server, the run files were converted from the MIDAS format to a file format readable by TScan. After this conversion was complete, the ADC spectra from the 14 detectors were summed and gain-matched using TScan to ensure peaks from all detectors were properly aligned before singles spectra and  $\gamma - \gamma$  coincidence matrices could be further analyzed. The steps involved in this process are illustrated in the flow chart shown in Figure 21.

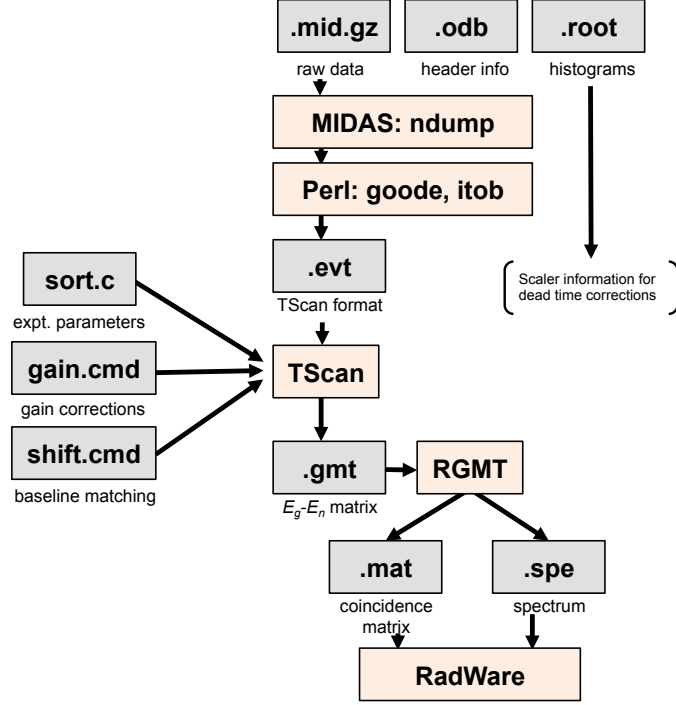


**Figure 21.** Flow chart describing the steps involved in the offline analysis of data from the GEANIE experiment. Grey boxes identify the input files, which contain data or parameters, used by the programs (shown in orange).

### Run file conversion to TScan format.

After the compressed MIDAS run files in the `.mid.gz` format were unzipped, they were dumped into a hexadecimal file using the MIDAS subroutine `ndump`. This hexadecimal file was then sent as input to the Perl scripts `goode` and `itob`, which converted the data into event files (`.evt`) readable by TScan. A BASH shell script was written to automate this process, which generally required 1-2 minutes to process each event file.

### TScan presort routine.

The TScan program was compiled from a presort routine `sort.c`, which contained the sorting parameters used to sum the data from each of the detectors into a matrix. The result of compiling the presort routine `sort.c` is the TScan

executable, which summed the numerous event files to produce a single 2-dimensional  $E_\gamma$  vs.  $E_n$  matrix in the `.gmt` file format. The single `.gmt` file contained all the spectral data from the experiment, formatted per the specifications defined in the presort routine.

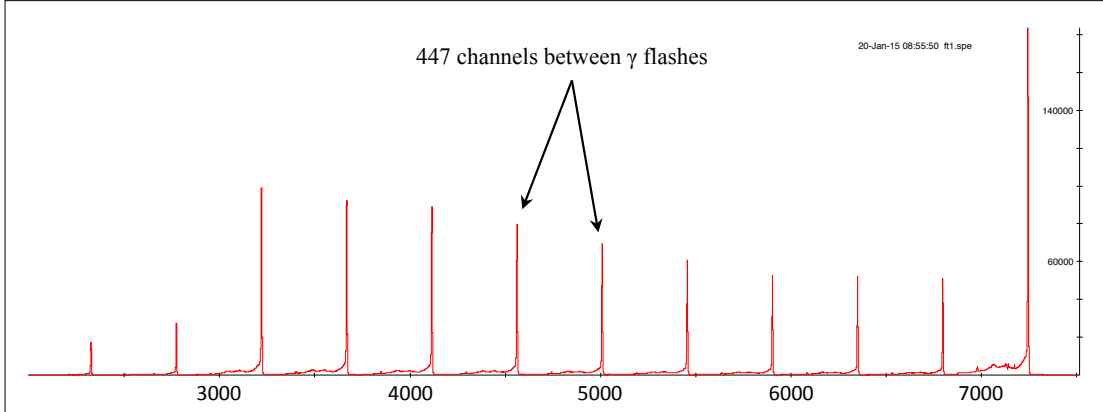
The conversion from neutron TOF to energy was included in the presort routine. This step involved application of the relativistic formula

$$E_n = \frac{E_0}{\sqrt{1 - v^2/c^2}}, \quad (12)$$

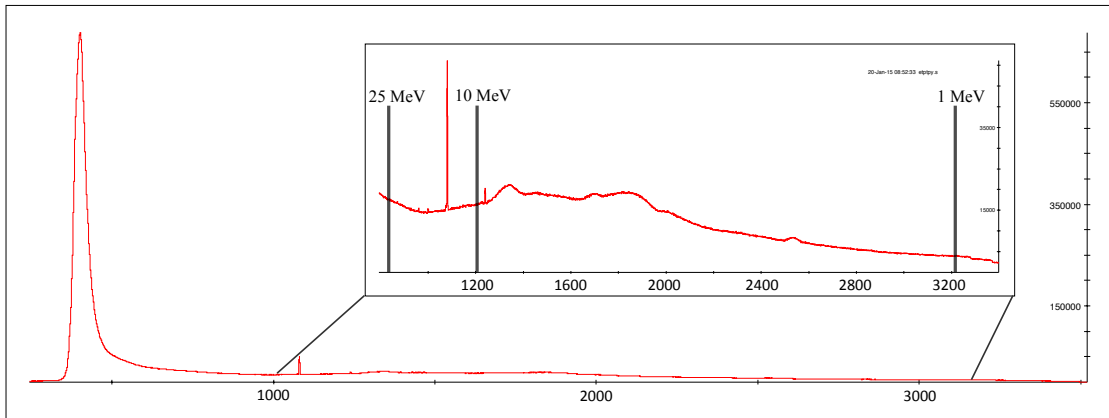
where  $E_0 = 939.57$  MeV is the neutron rest energy,  $v$  is the neutron velocity and  $c$  is the speed of light in a vacuum [14, 39]. Since the distance between the proton beam pick-off to the detector array was known to be 20.34 m, the neutron energy  $E_n$  could be deduced from the TOF. Also contained in the presort routine were the parameters necessary to align the TDC spectra from each detector to the same channel, so that this TOF-to- $E_n$  conversion was consistent across all the detectors.

TOF measurement involved a TDC measurement of the time between the start signal, generated by the proton beam pick-off, and the stop signal, which occurred upon the  $\gamma$  flash in the HPGe detectors from each micropulse. The TDC spectrum structure is shown in Figure 22(a). The TDC spectra from each detector exhibited a 447-channel periodicity according to the beam's constant micropulse spacing, which was used in the presort routine to calculate the neutron time of flight (TOF) that accompanies each  $\gamma$ -ray signal. The output from this step is the TOF spectrum shown in Figure 22(b).

The neutron energies  $E_n = 1, 10$  and  $25$  MeV highlighted in the inset of Figure 22(b) were calculated from the TOF using Equation 12.



(a) TDC spectrum



(b) TOF spectrum

**Figure 22.** Time spectra generated by the planar detectors. The time spectra from the coaxial detectors are similar to those shown for the planar detectors. Panel (a) shows the raw TDC output from detector 1. The constant micropulse spacing in the TDC spectrum was used to collapse the TDC spectra into the neutron time-of-flight spectrum shown in panel (b), which includes the TDC data from all the planar detectors. The neutron energies at which the gates were applied in the data analysis are represented by the vertical lines in the inset. The single-channel wide vertical spike at channel 1080 is a spurious signal generated by the TDC hardware, and must be corrected when calculating dead time corrections.

### Gain matching.

The ADCs output  $\gamma$ -ray energies ( $E_\gamma$ ) in terms of counts per channel, and had to be gain-matched to ensure peaks from each detector were aligned at the same channel. Due to the different hardware gain settings for the planar and coaxial

detectors, the two detector types were gain-matched separately. The gain matching procedure was complicated by the fact that over the month-long experiment the gain for certain detectors drifted by significant amounts.

The gain matching was performed iteratively using small subsets of the data to insure against significant gain and baseline drifts that might result in unacceptable peak broadening. After summing the events from 20-30 event files into a single `.gmt` matrix file, the matrix was parsed using the `RGMT` (read `.gmt`) subroutine from TScan into one-dimensional  $\gamma$ -ray spectrum (`.spe`) files. These spectra were examined for each of the 14 detectors using the `gf3` program from the RadWare package. The peak locations by channel were recorded and used to generate corrected gain and baseline parameters according to the following formulas [40]:

$$\text{Gain} = \frac{y_2 - y_1}{x_2 - x_1} \quad (13)$$

$$\text{Shift} = y_2 - \text{Gain} \times x_2.$$

Here  $x_1$  and  $x_2$  are the channel locations of two peaks in the spectrum with known energy, while  $y_1$  and  $y_2$  are the desired channel locations of those peaks in the reference spectrum. For the gain matching of the planar detectors, the reference peaks selected were the 61.14 keV  $K_{\alpha 1}$  X-ray from rhenium (see Table 6) and the 511 keV annihilation peak, which were assigned reference locations based on a gain of 8.192 channels/keV. The peaks used for gain matching the coaxial detectors were the 134.247 keV  $\gamma$ -ray from  $^{187}\text{Re}$  and the 511 keV  $e^+e^-$  annihilation peak, using a reference gain of 2.048 channels/keV. The corrected parameters for each subset of the data were provided as input to TScan using the files `gain.cmd` and `shift.cmd` before summing the subsets into a single master `.gmt` matrix.

### **Singles spectra and coincidence matrices.**

The RGMT program, as described above, generated one-dimensional  $\gamma$ -ray spectra from the final `.gmt` matrix. The spectra generated in this way included individual ADC spectra for each of the 14 detectors, as well as summed spectra incorporating the counts from all of the planar or coaxial detectors. The summed spectra, provided the gain matching was performed properly, resulted in the best counting statistics and thus the best opportunity for observation of new  $\gamma$ -ray transitions. These summed spectra, gated on selected neutron energy ranges as described in Section 4.2, were the focus of the data analysis.

Included in the TScan program is an executable `gmt2mat` for extracting from the `.gmt` matrix  $\gamma - \gamma$  coincidence matrices in the `.mat` format preferred by RadWare. The RadWare distribution includes a program `escl18r` that is designed to examine these 2-dimensional coincidence matrices and produce level schemes from the coincidence data.

### **Neutron Energy Gates.**

Gates on the neutron energies were specified in the TScan presort routine `sort.c` to generate ADC spectra showing  $\gamma$ -rays that originated primarily from  $(n, n'\gamma)$  or  $(n, 2n\gamma)$  reactions, according to the thresholds of the cross sections plotted in Figure 12. The neutron energy gates used to select  $\gamma$ -rays that originated from the  $^{187}\text{Re}(n, n'\gamma)^{187}\text{Re}$  reaction channel were  $1.0 \leq E_n \leq 10$  MeV. For the  $^{187}\text{Re}(n, 2n\gamma)^{186}\text{Re}$  reaction channel, Figure 12 identifies that this reaction dominates the  $(n, n'\gamma)$  and  $(n, 3n\gamma)$  reactions in the energy range  $10 \leq E_n \leq 18$  MeV. Gates of  $10 \leq E_n \leq 25$  MeV were chosen to increase the number of counts in each channel, and known  $\gamma$ -ray peaks due to  $^{185}\text{Re}$  were subtracted out to leave only contributions from  $^{186}\text{Re}$ .

The  $1.8 \mu\text{s}$  delay between micropulses is a sufficiently long time for the high-energy neutrons from one of the sub-nanosecond micropulses to overtake the low-energy neutrons from a previous micropulse, an effect known as frame overlap [32]. This must be accounted for in the data analysis by selection of an appropriate neutron low-energy cutoff of 650 keV or greater. For this experiment, the low-energy cutoff chosen was 1.0 MeV, which was sufficient to select out the slow neutrons that would be subject to frame overlap and remove any ambiguity in the neutron energy. This low-energy cutoff also had the effect of eliminating  $\gamma$ -rays produced in the  $^{187}\text{Re}(n, \gamma)^{188}\text{Re}$  reaction channel, because the  $(n, \gamma)$  cross section is negligible compared to that of the  $(n, n')$  reaction at neutron energies above 1 MeV.

With the neutron energy gates set as described above, the neutron energy bins in the  $E_\gamma$  vs.  $E_n$  matrix were projected onto the  $E_\gamma$  axis to generate summed projection spectra consisting only of  $\gamma$ -rays correlated to neutrons in the desired energy ranges. These projection spectra are shown in Figures 23 and 24 for the planar and coaxial detectors, respectively.

### Energy Calibration.

Energy calibration was performed using the **Source** and **ENCAL** executables from the RadWare software package. The primary calibration source for both planar and coaxial detectors was  $^{152}\text{Eu}$ . Because of the different gain settings for the two detectors, different  $\gamma$ -ray peaks were used for the two calibrations: 7 peaks with energies between 121 keV and 867 keV were used for the planar detector calibration, while 10 peaks with energies ranging from 121 keV to 1408 keV were used to calibrate the coaxial detector spectrum. The **ENCAL** subroutine produced planar and coaxial calibration files based on linear least-squares fits to the known-energy peaks in  $^{152}\text{Eu}$ . Further analysis is required to quantify the errors inherent in the energy

calibration process, although they were estimated to be on the order of 0.1 keV.

### Peak Fitting in RadWare (gf3).

Peaks in the projection spectra were fitted using the least-squares peak fitting algorithm in gf3. The gf3 program is specifically designed for analysis of  $\gamma$ -ray spectra produced by HPGe detectors, and it fits peaks according to the unique response function of an HPGe detector [41]. For this experiment, each peak was fitted with a pure Gaussian and peak centroid errors due to the fitting process were quantified. These errors are reflected in Tables 2 through 5. Counts under each peak were determined by subtracting the background, estimated over a range of channels bounding the peak.

### 4.3 Projection Spectrum Analysis

Of primary interest in this experiment was evidence of transitions feeding the 149(7) keV isomer in  $^{186}\text{Re}$ , though new transitions in  $^{187}\text{Re}$  were also sought. Peaks in the projection spectra, gated on the neutron energies described in Section 4.2, were fitted using gf3, and the energies of these peaks were compared with known  $\gamma$ -ray transitions listed in the ENSDF [10].

## Planar Detector Projection Spectra.

The projection spectrum obtained from the planar detectors included  $\gamma$ -rays with energies in the range  $0 \leq E_\gamma \leq 1.0$  MeV. Figure 23 shows the summed planar spectrum over the energy range  $10 \leq E_\gamma \leq 900$  keV, outside of which there are no significant spectral features.

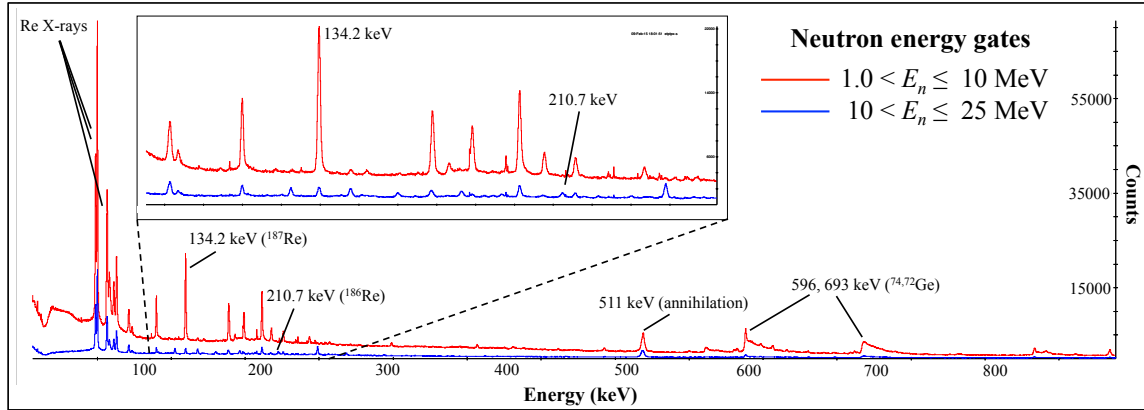


Figure 23. Summed planar detector spectrum plotted by gf3, showing the energies of selected prominent peaks from rhenium isotopes and sources of background. The horizontal axis identifies the  $\gamma$ -ray energy in keV according to the energy calibration applied. The vertical axis is the total number of counts per channel, where the conversion gain results in 8.192 channels per keV. The 134.2 keV peak from  $^{187}\text{Re}$  and the 210.7 keV peak due to  $^{186}\text{Re}$  are identified to show the effects of gating on the different neutron energies.

$^{187}\text{Re}(n, n'\gamma)^{187}\text{Re}$  reaction channel.

The  $\gamma$ -rays from the  $^{187}\text{Re}(n, n'\gamma)^{187}\text{Re}$  reaction channel were selected by gating on neutron energies in the range of 1.0 MeV to 10.0 MeV. The peaks in the resulting spectra are cataloged in Table 2.

**Table 2.** Peaks observed in planar detectors with  $1.0 \leq E_n \leq 10.0$  MeV attributed to  $^{187}\text{Re}$ . These included 1 not previously reported in the literature for  $^{187}\text{Re}$  (identified in red).

Energy (keV)	Fit Error	Database Energy (keV)	Area (counts)	Error
72.58	0.01	72.002	33212	590
134.47	0.00	134.247	155581	473
170.05	0.00	168.5	72892	376
182.48	0.00	182.3	56029	350
205.15	0.01	204.9	24194	293
214.95	0.01	214.8	19729	279
236.54	0.01	236.4	15704	266
304.15	0.02	304	7590	237
374.78	0.02	374.7	7261	225
404.26	0.03	404	4984	214
441.60	0.05	441.3	2446	444
479.44	0.02	479.53	9047	222
586.48	0.04	586.3	6057	549
588.83	0.02	589.06	10463	666
618.11	0.02	618.37	9713	250
647.27	0.04	647.3	4838	204
682.26	0.05	682.34	3637	224
685.64	0.03	685.81	6645	263
<b>719.31</b>	<b>0.07</b>	<b>None assigned</b>	<b>3376</b>	<b>218</b>
745.17	0.09	745.21	2866	199
772.60	0.06	772.87	4101	191
843.18	0.04	842.1	11552	518
846.57	0.09	844.7	4852	428

**$^{187}\text{Re}(n, 2n\gamma)^{186}\text{Re}$  Reaction Channel.**

The  $\gamma$ -rays from the  $^{187}\text{Re}(n, 2n\gamma)^{186}\text{Re}$  reaction channel were selected by gating on neutron energies in the range of 10.0 MeV to 25.0 MeV. The peaks in the resulting spectra are cataloged in Table 3.

**Table 3.** Peaks observed in planar detectors with  $10.0 \leq E_n \leq 25.0$  MeV attributed to  $^{186}\text{Re}$ . These included 4 not previously reported in the literature for  $^{186}\text{Re}$  (identified in red).

Energy (keV)	Fit Error	Database Energy (keV)	Area (counts)	Error
144.37	0.01	143.919	10046	287
210.83	0.02	210.685	4146	141
232.41	0.07	232.1	1224	123
<b>266.85</b>	<b>0.02</b>	<b>None assigned</b>	<b>5394</b>	<b>137</b>
316.54	0.05	316.473	1577	106
<b>354.31</b>	<b>0.09</b>	<b>None assigned</b>	<b>818</b>	<b>96</b>
<b>381.24</b>	<b>0.06</b>	<b>None assigned</b>	<b>1239</b>	<b>95</b>
413.54	0.06	413.21	527	87
<b>492.64</b>	<b>0.12</b>	<b>None assigned</b>	<b>1424</b>	<b>243</b>

## Coaxial Detector Projection Spectra.

The projection spectrum obtained from the coaxial detectors included  $\gamma$ -rays with energies in the range  $0 \leq E_\gamma \leq 4.0$  MeV. Figure 24 shows the summed planar spectrum over the energy range  $50 \leq E_\gamma \leq 3750$  keV, outside of which there are no significant spectral features.

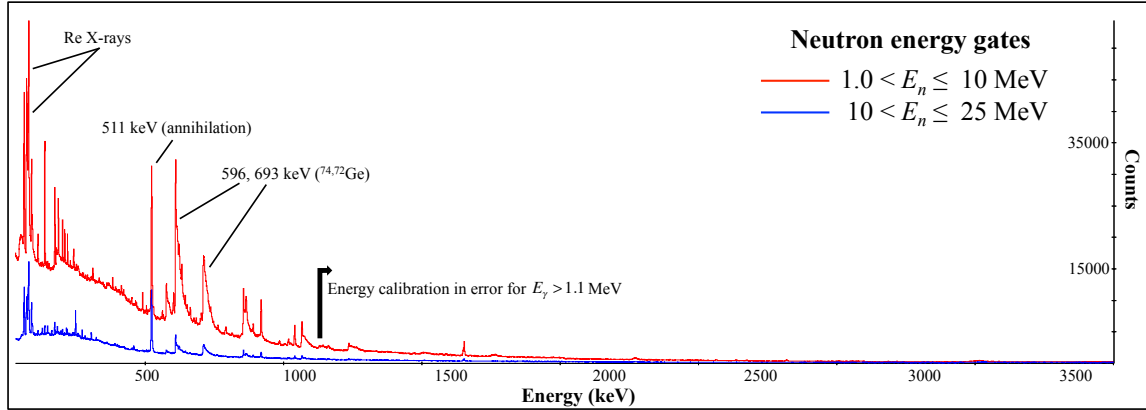


Figure 24. Summed coaxial detector spectrum plotted by gf3, showing the energies of selected prominent peaks from rhenium isotopes and sources of background. The horizontal axis identifies the  $\gamma$ -ray energy in keV according to the energy calibration applied. The vertical axis is the total number of counts per channel, where the conversion gain results in 2.048 channels per keV. No peaks are identified at energies greater than 1.1 MeV due to energy calibration errors that resulted from ADC gain nonlinearities.

**$^{187}\text{Re}(n, n'\gamma)^{187}\text{Re}$  Reaction Channel.**

The  $\gamma$ -ray peaks from the  $^{187}\text{Re}(n, n'\gamma)^{187}\text{Re}$  reaction are listed in Table 4.

**Table 4.** Peaks observed in coaxial detectors with  $1.0 \leq E_n \leq 10.0$  MeV attributed to  $^{187}\text{Re}$ . These included 4 not previously reported in the literature for  $^{187}\text{Re}$  (identified in red).

Energy (keV)	Fit Error	Database Energy (keV)	Area (counts)	Error
134.76	0.01	134.247	70187	433
170.20	0.01	168.5	48871	401
182.57	0.01	182.3	46003	396
205.19	0.02	204.9	26611	366
214.90	0.02	214.8	21064	359
236.43	0.04	236.4	11405	351
304.00	0.09	304	8975	405
374.33	0.06	374.7	12350	382
404.07	0.07	404	11353	371
440.78	0.00	441.3	6365	657
454.86	0.28	454.92	2483	334
478.95	0.06	479.53	10730	338
492.20	0.20	491.2	3299	320
516.57	0.05	518.6	13566	336
585.94	0.05	586.3	7199	296
588.23	0.03	589.06	14569	346
617.47	0.04	618.37	17871	507
635.96	0.19	635.8	3268	355
646.74	0.05	647.3	12222	351
<b>659.84</b>	<b>0.07</b>	<b>None assigned</b>	<b>7375</b>	<b>310</b>
681.76	0.06	682.34	4313	535
685.04	0.05	685.81	7773	585
<b>718.97</b>	<b>0.08</b>	<b>None assigned</b>	<b>4335</b>	<b>536</b>
744.45	0.09	745.21	5831	432
771.71	0.07	772.87	8456	520
843.46	0.04	842.1	26194	766
960.96	0.10	960.17	5133	591
<b>992.45</b>	<b>0.07</b>	<b>None assigned</b>	<b>5964</b>	<b>224</b>
<b>1014.50</b>	<b>0.02</b>	<b>None assigned</b>	<b>25076</b>	<b>275</b>

### $^{187}\text{Re}(n, 2n\gamma)^{186}\text{Re}$ Reaction Channel.

The  $\gamma$ -rays from the  $^{187}\text{Re}(n, 2n\gamma)^{186}\text{Re}$  reaction channel were selected by gating on neutron energies in the range of 10.0 MeV to 25.0 MeV. The peaks in the resulting spectra are cataloged in Table 5.

**Table 5.** Peaks observed in coaxial detectors with  $10.0 \leq E_n \leq 25.0$  MeV attributed to  $^{186}\text{Re}$ . These included 3 not previously reported in the literature for  $^{186}\text{Re}$  (identified in red).

Energy (keV)	Fit Error	Database Energy (keV)	Area (counts)	Error
144.58	0.04	143.919	4062	170
210.78	0.04	210.685	3612	169
232.32	0.10	232.1	1498	160
251.84	0.11	251.841	1396	163
<b>266.58</b>	<b>0.03</b>	<b>None assigned</b>	<b>4511</b>	<b>227</b>
316.49	0.15	316.473	3083	215
<b>380.94</b>	<b>0.16</b>	<b>None assigned</b>	<b>2470</b>	<b>190</b>
390.30	0.19	390.91	2032	186
<b>629.65</b>	<b>0.13</b>	<b>None assigned</b>	<b>1258</b>	<b>180</b>

### Peaks Above 1.1 MeV.

Other unassigned peaks with  $E_\gamma > 1.1$  MeV existed in the coaxial detector spectra in both reaction channels, however, these peaks were not attributed to the rhenium isotopes in this work. This was due to the fact that based on certain  $\gamma$ -rays in the ENSDF, the energy calibration at  $\gamma$ -ray energies above 1.1 MeV was observed to be in error greater than 5 keV. Apparent nonlinearities in the coaxial detector gain resulted in difficulty identifying new transitions from known sources of background, primarily those  $\gamma$ -rays due to  $(n, xn\gamma)$  reactions in germanium isotopes. This anomalous behavior persisted despite numerous attempts to calibrate the coaxial detector spectra using polynomials of orders 1 through 4 to fit the peaks in the  $^{152}\text{Eu}$  source spectrum.

## Common Spectral Features.

Both coaxial and planar detector spectra include X-rays due to rhenium and bismuth, the electron-positron annihilation peak at 511 keV, and neutron induced pulses due to the direct interaction of neutrons with the germanium and bismuth nuclei in the detectors.

### X-rays.

X-rays from both rhenium and bismuth (present in the BGO suppression shields) are evident in both the coaxial and planar detector spectra. These X-rays originate from internal conversion in the target or detection medium, because an X-ray cascade follows the emission of an inner atomic shell electron. The X-rays are generally more intense than the  $\gamma$ -rays due to neutron-induced reactions, so the 61.14 keV  $K\alpha_1$  X-ray from rhenium in particular was used as the primary low-energy reference peak in the gain matching procedure for the planar detectors.

**Table 6. Energies of rhenium and bismuth X-rays evident in both planar and coaxial detector spectra. Values shown here are those published in the Lawrence Berkeley Lab X-ray Data Booklet [42].**

Element, X-ray	Energy (keV)
Rhenium, $K\alpha_2$	59.7179
Rhenium, $K\alpha_1$	61.1403
Rhenium, $K\beta_1$	69.31
Rhenium, $K\beta_2$	71.232
Bismuth, $K\alpha_2$	74.8148
Bismuth, $K\alpha_1$	77.1079
Bismuth, $K\beta_1$	87.343
Bismuth, $K\beta_2$	89.83

### **511 keV annihilation peak.**

The 511 keV peak present in all the spectra is due to electron-positron annihilation following pair production in the detection medium. Gamma rays with energies greater than 1.022 MeV can interact in the detector and result in the production of an electron-positron pair. This process must occur within the Coulomb field of a nucleus, and the cross section for pair production generally increases with  $Z^2$ , where  $Z$  is the atomic number of the detection material [43]. The electron and positron depart the location where they are created with some forward momentum, dependent on the energy of the  $\gamma$ -ray from which they originate. The positron, which travels a short distance inside the detection medium before encountering an electron, annihilates with the creation of two photons. Peaks at 511 keV and 1022 keV are evident in the HPGe spectra, indicative of when one or both of these two photons are detected. As these photons are often detected at distinct times according to the time resolution of the HPGe detector, the 511 keV peak is significantly more prominent than the 1022 keV sum peak [43].

Because of the momenta of both the positron and electron upon annihilation, the relative velocity of the particles is generally some significant fraction of the speed of light  $c$ , and the annihilation peak is Doppler-broadened as a result. Compared to other  $\gamma$ -ray peaks in the ADC spectra from the planar and coaxial detectors in this experiment, the 511 keV peak is significantly wider. Since the 511 keV peak was clearly evident in all the spectra, it was used for gain matching, and had to be carefully fitted to account for its unique Doppler-broadened shape.

### **Neutron-induced pulses.**

Fast neutron interactions in the germanium detection medium result in characteristically wide ramp-shaped peaks, primarily at  $\gamma$ -ray energies of

596.06, 609.0 and 693.4 keV. The first 2 of these 3 peaks are due to  $(n, n'\gamma)$  reactions in  $^{74}\text{Ge}$ , while the third is due to an  $(n, n'\gamma)$  reaction in  $^{72}\text{Ge}$ . When a fast neutron scatters off a germanium nucleus, energy goes into both nuclear recoil and excitation energy, the latter of which is released in  $\gamma$ -decay. Electron-hole pairs in the detector are created both by the  $\gamma$ -ray and the recoiling germanium nucleus, which broadens the peak on the high-energy side. Other background contributions included neutron-induced pulses from  $^{209}\text{Bi}$  and  $^{19}\text{F}$  in the BGO detectors and sample holder, respectively.

#### 4.4 $\gamma - \gamma$ Coincidence Matrix Analysis

The TScan presort routine `sort.c` was modified to include definitions for two  $\gamma - \gamma$  coincidence matrices gated on the neutron energies in the ranges  $1.0 \leq E_n \leq 10$  MeV and  $10 \leq E_n \leq 25$  MeV to select out those  $\gamma$ -ray events from the  $(n, n'\gamma)$  and  $(n, 2n\gamma)$  reaction channels, respectively. The resulting `.gmt` matrix file was converted to the RadWare `.mat` coincidence matrix format using the `gmt2mat` subroutine.

#### **RadWare `escl8r` program.**

The `escl8r` program included with the RadWare distribution reads symmetric 2-dimensional  $\gamma - \gamma$  coincidence matrices and allows the user to gate on peaks in the spectra to see other  $\gamma$ -rays in coincidence with the selected  $\gamma$ -ray. In this way, `escl8r` can be used to deduce more information about the level scheme for a given nucleus than can be found from an analysis of only singles  $\gamma$ -ray spectra.

### **Search of Coincidence Data for New Transitions.**

The relevant  $\gamma - \gamma$  coincidence matrices were searched for evidence of  $\gamma$ -ray cascades involving each of the new transitions discovered in the  $(n, n'\gamma)$  and  $(n, 2n\gamma)$  reaction channels described in Section 4.3. However, at each new transition energy, gating on the peak resulted in a complete absence of other  $\gamma$ -rays in coincidence with the selected peak energy. This observation implies a possibility that none of the new transitions proposed in this work are part of a  $\gamma$ -ray cascade, or that there is an absence of coincidence data from which one can make any determination about  $\gamma$ -ray cascades in the  $^{186}\text{Re}$  and  $^{187}\text{Re}$  nuclei. An examination of other prominent peaks in the spectra, such as the 134 keV peak in  $^{187}\text{Re}$ , supports the second hypothesis.

### **4.5 New $\gamma$ -ray Transitions in $^{187}\text{Re}$**

Tables 2 and 4 include 4 peaks attributed to  $^{187}\text{Re}$  not found in the ENSDF or XUNDL nuclear databases.

#### **659.84(7) keV.**

The 659.84 keV peak observed in the coaxial spectrum has a low intensity. It was not discernible above background in the planar spectrum, because the planar detectors have a lower detection efficiency than the coaxial detectors at  $\gamma$ -ray energies above  $\sim 400$  keV. This peak is possible evidence of an  $E1$  transition between the  $J^\pi = (1/2^-, 3/2^+, 5/2^-)$  level at 1661(6) keV to the  $J^\pi = (5/2^-, 7/2^+)$  level at 1000.93(12) keV, which would have a calculated energy of 658(6) keV per the ENSDF. The existence of the 1000.93 keV level, however, is listed as uncertain in the ENSDF.

### **719.1(2) keV.**

Peaks appear at energies of 718.97(8) keV in the coaxial spectrum and 719.31(7) keV in the planar spectrum, which average to 719.1(2) keV. These peaks may indicate the existence of an *M*1 or *E*2 transition between the  $J^\pi = (3/2^+, 5/2^+)$  level at 1230.10(4) keV to the  $J^\pi = 1/2^+$  level at 511.768(7) keV. Such a transition would have a calculated energy of 718.35(4) keV per the ENSDF, implying a discrepancy of 0.8 keV between the observed and calculated values for the energy. The ENSDF shows a *E*2 transition from the 511.768 level directly to the ground state, but there is no such transition evident in the  $\gamma - \gamma$  coincidence data.

An alternative possibility is that the peak at 719.1 keV is due to a previously unobserved transition from the uncertain 718.73(4) keV level (spin-parity unassigned) to the ground state ( $J^\pi = 5/2^+$ ).

### **992.45(7) keV.**

A 992.45 keV peak was observed in the coaxial detector spectrum. It is possible that it is evidence of a transition from the  $J^\pi = (9/2^-)$  level at 1200(3) keV in the ENSDF to the  $J^\pi = 9/2^-$  level at 206.252(7) keV, which has a calculated energy of 994(3) keV. However, such a transition would imply that the spin-parity assignment of  $J^\pi = (9/2^-)$  for the upper level is in error, as monopole ( $L = 0$ ) transitions in which a single photon is emitted are forbidden by parity selection rules [14]. The absence of a coincident 206.25 keV  $\gamma$ -ray in the data is explained by the fact that the 206.25 keV level in  $^{187}\text{Re}$  has a lifetime of 552.3 ns, and decay from this level to the ground state is highly converted ( $\alpha = 3.35$ ).

### **1014.50(2) keV.**

The 1014.50(2) keV peak observed in the coaxial spectrum leads to the possibility of a transition between the level at 1220.80(25) keV (spin-parity unassigned) to the  $J^\pi = 9/2^-$  level at 206.252(7) keV. Such a transition would have a calculated energy of 1014.55(25) keV. As in the case of the 992.52 keV transition above, no 206.252 keV  $\gamma$ -ray is evident in the coincidence data, likely due to the lifetime of the 206.25 keV level and internal conversion.

## **4.6 New $\gamma$ -ray Transitions in $^{186}\text{Re}$**

Noted in Tables 3 and 5 are 5 peaks attributed to  $^{186}\text{Re}$  that are not included in the ENSDF or XUNDL nuclear databases, or the associated literature. Of greatest significance is the 266.7 keV  $\gamma$ -ray observed in the planar spectrum that is expected to directly feed the  $2 \times 10^5\text{y}$  isomer. Each transition is described in greater detail in the following sections.

The level schemes of  $^{184}\text{Re}$  and  $^{186}\text{Re}$  show certain similarities at low energies, owing to the fact that both isotopes have long-lived isomers in the 140 - 190 keV energy range with matching fully aligned  $\pi d_{5/2} \otimes \nu i_{11/2}$  configurations [1, 31]. The known level structure above the 188 keV isomer in  $^{184}\text{Re}$  provided motivation for the assignment of transitions that feed the isomer in  $^{186}\text{Re}$ . In  $^{184}\text{Re}$ , three primary transitions that feed the isomer are known; these are shown in Figure 25 alongside known levels and proposed transitions in  $^{186}\text{Re}$ .

### **266.7(2) keV.**

The 266.7(2) keV  $\gamma$ -ray is the average energy of peaks at 266.85(2) keV and 266.58(3) keV in the planar and coaxial spectra, respectively. This  $\gamma$ -ray is a candidate for a transition that directly feeds the isomer at 149(7) keV from the level

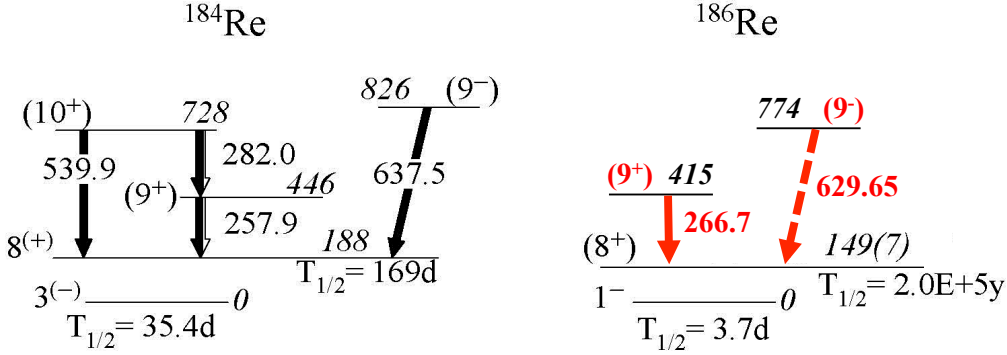


**Figure 25.** Extracts from the  $^{184}\text{Re}$  and  $^{186}\text{Re}$  level schemes, showing similarities in the spin-parity assignments for levels in the two nuclei, and proposed transitions identified in this experiment shown in red. The 629.65 keV transition is dashed to highlight the fact that this is one of two possibilities for a transition of this energy. Adapted with permission from [1].

at 414.9(5) keV proposed in [26]. Wheldon and others state that the 414.9 keV level observed in the group's experiment involving the population of  $^{186}\text{Re}$  levels via the  $^{187}\text{Re}(p, d)^{186}\text{Re}$  reaction may have a spin-parity of  $J^\pi = 7^-$ , though this assignment is only tentative. Here, the similarity between the levels in  $^{184}\text{Re}$  and  $^{186}\text{Re}$  motivates a tentative assignment of  $J^\pi = (9^-)$  for the spin-parity of the 414.9 keV level. Furthermore, existence of this transition implies an energy of  $414.9(5) - 266.7(2) = 148.2(5)$  keV for the isomer, a significant improvement over the  $149 \pm 7$  keV value originally deduced by Seegmiller, et al. [7].

### 354.31(9) keV.

The low-intensity 354.31 keV peak observed in the planar spectrum was not discernible above background in the coaxial detector spectrum. This peak is likely indicative of an  $E1$  transition between the  $J^\pi = (4)^+$  level at 500.722(16) keV to the  $J^\pi = (3)^-$  level at 146.274(4) keV, which would have a calculated energy of 354.448(16) keV per the ENSDF.

### **381.1(2) keV.**

Peaks appear at energies of 381.24(6) keV in the coaxial spectrum and 380.94(16) keV in the planar spectrum, which average to 381.1(2) keV. These peaks likely represent evidence of a  $E1$  transition from the  $J^\pi = (5)^+$  level at 559.976(9) keV in the ENSDF to the  $J^\pi = (6)^-$  level at 180.1(5) keV proposed by Wheldon and others [26]. This transition would have a calculated energy of 379.9(5) keV per the ENSDF.

### **492.64(12) keV.**

The 492.64 keV peak observed in the planar spectrum was not discernible above background in the coaxial spectrum. This peak is likely indicative of an  $M1$  transition between the  $J^\pi = (2^-, 3^-)$  level at 1069.8 keV to the  $J^\pi = (2^-)$  level at 577.732(16) keV, which would have a calculated energy of 492.077(16) keV per the ENSDF. Existence of such a transition would give credence to a tentative assignment of  $J^\pi = (3^-)$  to the 1069.8 keV level, as parity selection rules prohibit monopole ( $L = 0$ ) transitions in which a single photon is emitted [14].

### **629.65(13) keV.**

Motivated by the  $^{184}\text{Re}$  level scheme shown in Figure 25, the 629.65 keV transition observed in the  $^{187}\text{Re}(n, 2n\gamma)^{186}\text{Re}$  channel is possibly a transition from the 774.2(15) keV level observed by Wheldon and others that directly feeds the  $2 \times 10^5$  y isomer. This level is not strongly populated in the  $^{187}\text{Re}(p, d)^{186}\text{Re}$  reaction per Wheldon and others, and no proposed spin-parity is given in the group's 2009 paper [26]. Per the same reasoning as in the case of the 267 keV peak, a spin-parity of  $J^\pi = 9^-$  is likely for this state, as shown in Figure 25. Existence of this transition would imply an energy of  $774.2(15) - 629.65(13) = 144.6(15)$  keV for

the isomer, which differs from the 148.2(5) keV value deduced above by more than one standard deviation.

Alternatively, the observed 629.65 keV transition could be evidence of an  $M1$  transition from the  $J^\pi = (1^-)$  level at 689.3 keV to the  $J^\pi = (2)^-$  level at 59.010 keV, which would have a calculated energy of 630.29 keV.

## V. Future Work

The results claimed in this work represent the conclusions from an initial analysis of the data. Remaining tasks in the data analysis include calculating  $\gamma$ -ray excitation functions and transition cross sections for new transitions, and comparing these cross sections with those calculated using nuclear reaction codes.

### 5.1 Excitation Functions

The  $\gamma$ -ray excitation function  $X_\gamma(E_n)$  is defined as the  $\gamma$ -ray yield at a given energy divided by the neutron flux:

$$X_\gamma(E_n) = \frac{I_\gamma(E_n)}{\Phi(E_n)}. \quad (14)$$

Here,  $I_\gamma$  is  $\gamma$ -ray intensity in photons/s and  $\Phi$  is the neutron flux in neutrons/MeV·s. The excitation function for a given  $\gamma$ -ray is proportional to the partial  $\gamma$ -ray cross section, as described in Section 5.2. Obtaining the  $\gamma$ -ray excitation functions for the new transitions claimed in this work will provide a basis for an initial comparison with theoretical models. These models, described in further detail in Section 5.3, are capable of producing partial  $\gamma$ -ray cross sections, so the shapes of the curves can be compared. Based on the goodness of fit between the shapes of the experimentally obtained  $\gamma$ -ray excitation functions and the partial  $\gamma$ -ray cross sections produced by the models, it may be possible to deduce transition multipolarities and spin-parity assignments for certain levels.

### 5.2 Transition Cross Section Calculations

Gamma-ray excitation functions, which are defined as the  $\gamma$ -ray intensity  $I_\gamma$  as a function of incident neutron energy  $E_n$  according to Equation 14, will be used to

develop cross sections for the newly-discovered transitions. The transition cross section  $\sigma(E_n)$  for a particular  $\gamma$ -ray energy  $E_\gamma$  is related to the excitation function  $X_\gamma(E_n)$  through the following relation [32, 34]:

$$\sigma(E_n) = X_\gamma(E_n) \cdot \frac{\text{DeadTime}_\gamma \cdot (1 + \alpha) \cdot C_\gamma(E_n)}{\text{DeadTime}_\Phi \cdot \epsilon(E_\gamma) \cdot t} \cdot N. \quad (15)$$

Here,

- $\text{DeadTime}_{\gamma,\Phi}$  is the dead time correction for the HPGe and fission chamber detectors, respectively,
- $\alpha$  is the conversion coefficient for the transition,
- $C_\gamma(E_n)$  is an angular correction factor,
- $\epsilon(E_\gamma)$  is the total efficiency of the detector array at the photon energy  $E_\gamma$ ,
- $t$  is the areal density of the target, in atoms/barn, and
- $N$  is a factor of normalization obtained by measuring the excitation function for a particular transition in  $^{56}\text{Fe}$ .

The methods for obtaining the 7 factors listed above necessary to arrive at the transition cross section from the excitation function are explained in the following sections.

### **Dead Time Corrections.**

Both the  $\gamma$ -ray and fission chamber ADC spectra must be corrected for dead time to obtain the number of counts in real time from each of the detector types. This is critical to being able to discern the actual neutron flux and  $\gamma$ -ray yields. The process of correcting for dead time involves comparing the detector live times

against outputs from the clock timing hardware, both of which are sent to scaler modules and incorporated into the MIDAS data acquisition system. The scaler data needed to calculate the fission chamber and HPGe detector dead time are contained in the ROOT histograms that were produced by the online MIDAS analyzer and saved to disk following the experiment.

### **Internal Conversion Coefficients.**

Internal conversion coefficients for some transitions are published in the ENSDF, though a search of the database identifies many transitions for which no such measurement of  $\alpha$  has been made. This is particularly true in the case of isotopes that have not been the focus of much research, such as  $^{186}\text{Re}$  [10]. When no measurement of the conversion coefficient for a particular transition exists in the database, theoretical models can be used to calculate  $\alpha$ . The online conversion coefficient calculator BrIcc, developed at the Australian National University, is one such model [23]. Given the atomic number  $Z$ , transition energy  $E_\gamma$  and transition multipolarity, the BrIcc code applies a Dirac-Fock computational model to account for electron vacancies in the process of internal conversion. It produces conversion coefficients that generally match experimental data to within several percent [44].

### **Detector Array Efficiency Calibration.**

The HPGe detectors in the GEANIE array were calibrated individually for efficiency using a variety of calibration sources, a process that took place during the run cycle.

### **Angular Correction for Efficiency.**

The absolute  $\gamma$ -ray detection efficiency of detectors in the GEANIE array is subject to angular variation due to the inherent multipolarity of the  $\gamma$ -rays emitted from the target and effects of self-absorption within the target. The product of these two individual factors is the angular correction factor  $C_\gamma$  in Equation 15.

### **Self-absorption effects.**

A certain percentage of  $\gamma$ -rays produced in the target are absorbed by the target before they can be detected. Assuming excited nuclear states are produced according to a uniform distribution within the target,  $\gamma$ -rays emitted from target nuclei must pass through varying amounts of target material before they can be detected. Correcting for this effect involves an Monte Carlo Neutral Particle (MCNP) simulation of the target and detector array [39, 45].

### **Multipolarity effects.**

The angular distribution of  $\gamma$ -rays produced in a target relative to the beam direction is described by the differential cross section  $\frac{d\sigma}{d\theta}$ , which is a superposition of even Legendre polynomials  $P_n(\sin \theta)$ , per the equation

$$\frac{d\sigma}{d\theta}(\theta) = \frac{\sigma_0}{4\pi} \sum_{n \text{ even}} a_n P_n(\sin \theta) \quad (16)$$

where  $\sigma_0$  is the total cross section,  $\theta$  is the scattering angle, and the  $a_n$  are the Legendre polynomial coefficients [34, 39]. The total cross section is calculated from the total detector array efficiency, and the individual detector locations listed in Table 1 provide the scattering angle  $\theta$ . A code known as AVALANCHE is available for performing these angular correction calculations given a set of parameters

defining the detector geometry.

### Normalization Using $^{56}\text{Fe}$ .

The normalization constant  $N$  in Equation 15 relates the excitation function to the transition cross section  $\sigma$ . This normalization constant is obtained by measuring the  $\gamma$ -ray yield for the 846.8 keV transition in  $^{56}\text{Fe}$  from the reaction  $^{56}\text{Fe}(n, n'\gamma)^{56}\text{Fe}$ . The cross section for this reaction is well known and its value at the neutron energy  $E_n = 14.5$  MeV is used as the normalization constant. Application of this normalization factor is necessary to correct for the differences in the sizes of the beam spot and the target.

## 5.3 Reaction Modeling

Two primary computational codes are available that model partial  $\gamma$ -ray cross sections, equal to the transition cross section divided by  $(1 + \alpha)$ , where  $\alpha$  is the internal conversion coefficient for the transition in question. These codes, COH<sub>3</sub> and TALYS 1.6, are commonly used to validate experimental data obtained at GEANIE [34, 35]. COH<sub>3</sub>, which was developed at LANSCE, calculates partial  $\gamma$ -ray cross sections for neutron-induced reactions. Both codes have been used to validate transition cross sections obtained from recent GEANIE experiments [34, 35, 37].

### COH<sub>3</sub>.

COH<sub>3</sub> is a C++ code developed at LANSCE by T. Kawano for the purpose of modeling nuclear reaction cross sections in mid- to high- $Z$  elements. It supersedes the earlier GNASH code, built for the same purpose and used to validate experimental cross sections prior to 2008. COH<sub>3</sub> is capable of producing differential  $\gamma$ -ray cross sections given neutron energies in the keV to MeV energy range, which

permit it to be used to validate cross sections obtained in this experiment. The theoretical models used to determine these cross sections are optical and Hauser-Feshbach statistical models, and the code applies these using a Monte Carlo algorithm [46, 47].

### TALYS.

The TALYS program is designed to model a variety of nuclear reactions in mid-to high- $Z$  elements in the energy range 1 keV – 200 MeV. TALYS, which is open-source software, was developed as part of a collaboration between the French Alternative Energies and Atomic Energy Commission (CEA) and the Nuclear Research and Consultancy Group (NRG) in the Netherlands. The code is used to simulate nuclear reactions for the purposes of analyzing experiments and generating nuclear data, including cross sections, in applications where there is insufficient experimental data [48]. The code relies on a number of nuclear reaction models, including the Hauser-Feshbach model that is also used in the COH<sub>3</sub> nuclear reaction code. TALYS is a FORTRAN-based program that generates cross sections and reaction  $Q$ -values given user input consisting of a deck of reaction parameters.

#### 5.4 Examination of Data from $^{nat}\text{Re}$ Runs

Similarities between the level structures of  $^{184}\text{Re}$  and  $^{186}\text{Re}$  suggest it is possible that the excitation functions for the transitions that feed the  $J^\pi = 8^+$  isomer in  $^{184}\text{Re}$  may be similar to those that feed the isomer in  $^{186}\text{Re}$ . To test this hypothesis, 24 hours of irradiation of sample of natural rhenium, which contains 37.4%  $^{185}\text{Re}$ , was accomplished on 8 – 9 December. The data obtained from these experimental runs will be used to obtain excitation functions for  $\gamma$ -rays produced by the  $^{185}\text{Re}(n, n'\gamma)^{185}\text{Re}$  and  $^{185}\text{Re}(n, 2n\gamma)^{184}\text{Re}$  reactions.

### **Excitation Functions in Thallium Isotopes.**

An analysis cross sections for the new transitions discovered in  $^{186}\text{Re}$  will follow the methodology used in a series of GEANIE experiments in 2007 – 2008, in which previously unknown transitions populating the  $J^\pi = 7^+$  isomer in  $^{204}\text{Tl}$  were identified. These experiments, which were designed to study the nuclear structure of  $^{204}\text{Tl}$ , identified several new transitions in  $^{204}\text{Tl}$  from the  $^{205}\text{Tl}(n, 2n\gamma)^{204}\text{Tl}$  reaction.

The existence of the  $7^+$  isomer in  $^{204}\text{Tl}$  was previously known, although the structure above the isomer was not [49]. Similarities between the level schemes of  $^{202}\text{Tl}$  and  $^{204}\text{Tl}$  led to the hypothesis that the structures above the isomer were similar [37]. Both  $^{202}\text{Tl}$  and  $^{204}\text{Tl}$  have a  $J^\pi = 7^+$  isomer with similar energies and half-lives. These similarities between the two isotopes suggested that the levels above the isomer in  $^{204}\text{Tl}$  were similar to those in  $^{202}\text{Tl}$ .

Excitation functions for new transitions observed in the  $^{205}\text{Tl}(n, 2n\gamma)^{204}\text{Tl}$  reaction channel were compared with those for the analogous transitions from spectra taken from the  $^{203}\text{Tl}(n, 2n\gamma)^{202}\text{Tl}$  reaction. The results showed similarities between the two sets of excitation functions. Evidence from modeling and other experiments led to the conclusion that for transitions with identical final level spin parity assignments, similar excitation function shapes implied the same initial level spin parity. This led to the tentative assignment of  $J^\pi = 7^+$ , for the 1454 keV level in  $^{204}\text{Tl}$  that populates the  $8^+$  isomer via a 349.9 keV direct transition.

### **Comparison of Rhenium Excitation Functions.**

Proceeding as in the case of the thallium isotopes, the data from the  $^{nat}\text{Re}$  runs will be used to obtain  $\gamma$ -ray excitation functions from the  $^{185}\text{Re}(n, 2n\gamma)^{184}\text{Re}$  reaction channel. The excitation functions for the known  $\gamma$ -ray transitions feeding the  $J^\pi = 8^+$  isomer in  $^{184}\text{Re}$  will be used with the excitation functions obtained

from the  $^{187}\text{Re}(n, 2n\gamma)^{186}\text{Re}$  reaction channel to motivate spin-parity assignments for levels above the isomer in  $^{186}\text{Re}$  [31].

## VI. Conclusion

The significant outcome of this experiment was enriching the level schemes of  $^{187}\text{Re}$  and  $^{186}\text{Re}$ . In particular, the structure above the  $2 \times 10^5$  y isomer in  $^{186}\text{Re}$  has not been proposed before, and new  $\gamma$ -ray transitions observed in the  $^{187}\text{Re}(n, 2n\gamma)^{186}\text{Re}$  reaction channel may be evidence of pathways by which the isomer is populated. One of these proposed transitions leads to an improved estimate of the excitation energy of the  $^{186m}\text{Re}$  isomer with a significantly smaller uncertainty than the value adopted in the literature.

### 6.1 Contributions to the Level Schemes of $^{187}\text{Re}$ and $^{186}\text{Re}$

The new transitions proposed here as a result of the preliminary analysis of the data from the November-December 2014 GEANIE experiment represent a contribution to the enrichment of the level schemes of both  $^{187}\text{Re}$  and  $^{186}\text{Re}$ . Though the primary focus of this research was on the nuclear structure of  $^{186}\text{Re}$ , 4 new levels were also observed in  $^{187}\text{Re}$ . Among the 5 new transitions discovered in  $^{186}\text{Re}$ , one was identified as feeding the  $2 \times 10^5$  y isomer in  $^{186}\text{Re}$ . If validated by nuclear reaction models, this will represent a substantial development towards understanding the structure above this especially long-lived isomer.

The absence of an observed cascade to the ground state from one of the possible high-spin states above the isomer would imply that any such decay mode has a low intensity relative to the transitions that populate the isomer. As a result, it is unlikely an intermediate state was discovered by which the isomer could be effectively depleted in the scheme described in Section 2.5.

## 6.2 Improved Estimate of $^{186m}\text{Re}$ Energy

The ENSDF database states the energy of the  $2 \times 10^5$  y isomer in  $^{186}\text{Re}$  is  $149 \pm 7$  keV above the ground state, the original energy proposed by Seegmiller and others in 1972 [7]. The observed  $\gamma$ -ray peak at  $267(1)$  keV in the  $^{187}\text{Re}(n, 2n\gamma)^{186}\text{Re}$  reaction channel is proposed in this work to be a transition to the isomer state from the  $414.9(5)$  keV level. This places the isomer energy at  $414.9(5) - 266.7(2) = 148.2(5)$  keV, which represents significant improvement over the  $149(7)$  keV value in the evaluated database.

## 6.3 Recommendations for Future Research

Calculating  $\gamma$ -ray excitation functions for the new transitions proposed in this work will permit an initial comparison of the experimental data with transition cross sections produced by the nuclear reaction codes Talys 1.6 and COH<sub>3</sub>. After excitation functions are obtained, transition cross sections can be calculated by applying corrections for detector dead time and efficiency, and these cross sections can be directly validated against theoretical models.

Data obtained from the experiment includes the results of 24 hours of irradiation of a natural rhenium target. Due to the presence of  $^{185}\text{Re}$  in the natural rhenium sample, these spectra include  $\gamma$ -rays produced via the  $^{185}\text{Re}(n, n'\gamma)^{185}\text{Re}$  and  $^{185}\text{Re}(n, 2n\gamma)^{184}\text{Re}$  reactions. From this data,  $\gamma$ -ray excitation functions from transitions in  $^{184}\text{Re}$  that are analogous to the ones proposed for  $^{186}\text{Re}$  may provide a basis for proposing spin-parity assignments in  $^{186}\text{Re}$ .

Following submission of this thesis document, the Ph.D. dissertation will continue to examine the data obtained from the GEANIE experiment, and the dissertation will include this additional data analysis, as described in Chapter V.

## Appendix A. Photoexcitation of $^{115m}\text{In}$ Using a Dynamitron Accelerator

Though not directly related to the rhenium experiment described in the body of the thesis, this appendix describes a demonstration of photoexcitation of nuclear isomers, which is analogous to the photodepletion scheme by which the  $^{186m}\text{Re}$  isomer could be induced to release its excess energy once a suitable intermediate state is discovered. The experiments described in this appendix also served the purpose of checking the energy calibrations of the Dynamitron accelerator at Wright State University (WSU) and the Varian L200 LINAC at the Army Research Laboratory (ARL). Both of these accelerators may be used in future studies involving nuclear isomers, so it is important that they are accurately calibrated.

Photoexcitation of nuclear isomers by  $(\gamma, \gamma')$  reactions is possible by irradiation with bremsstrahlung produced with an electron LINAC, according to the theory outlined in Section 2.5 of the thesis. In the experiment described in this appendix,  $^{115}\text{In}$  nuclei were excited to the 336 keV isomer  $^{115m}\text{In}$  via the  $^{115}\text{In}(\gamma, \gamma')^{115m}\text{In}$  reaction using the WSU Dynamitron operated at 1.2 MV.  $^{115m}\text{In}$   $\gamma$ -decays directly to the ground state with a half life of 4.486 hours, which allowed for measurement of the sample activity after irradiation in a HPGe detector at AFIT.

The results of the WSU/AFIT experiment were compared with those from a similar experiment involving a Varian L200A LINAC operated at a nominal voltage of 1.0 MV at the Army Research Laboratory (ARL) in Adelphi, MD. A significant difference in the  $^{115m}\text{In}$  yields achieved in the two experiments leads to the hypothesis that one of the two accelerators operated at an energy different from that stated.

By modeling the bremsstrahlung spectra from each experiment configuration using GEANT4, theoretical yields for the production of the  $^{115m}\text{In}$  isomer were

calculated from known cross sections for the  $^{115}\text{In}(\gamma, \gamma')^{115m}\text{In}$  reaction. By comparing the observed  $^{115m}\text{In}$  activities against the calculated values, it was possible to check the energy calibrations of the Dynamitron accelerator and the Varian LINAC.

## 1.1 Introduction

The Dynamitron at WSU can be used to produce bremsstrahlung photons via a tungsten converter with endpoint energies up to 1.2 MeV. The advantage of the Dynamitron is the relatively high current ( $\leq 10 \mu\text{A}$ ) that it can achieve compared to that of a van de Graaf accelerator, as well as its continuously tunable energy. The facility at WSU is thus capable of investigating the population and depletion of nuclear isomers by low energy ( $\gamma, \gamma'$ ) reactions.

Depending on the particular nucleus, a given isomer might be fed by numerous intermediate states, and there may be a host of photon energies that can be used in photoexcitation experiments. In the case of  $^{115}\text{In}$ , the first three IS's that feed the 336 keV isomer are the  $J^\pi = 7/2^+$  state at 934 keV, the  $J^\pi = 5/2^+$  state at 941 keV and the  $J^\pi = 11/2^+$  state at 1078 keV. Between 1.1 MeV and 3.0 MeV, there are at least five others [17].

Given the partial level scheme shown above, it is possible to deduce the integrated cross sections for inelastic photon excitation using Equation 8. To do so, however, the lifetime of the 597 keV level is required, and the ENSDF provides only an upper limit of  $\tau \leq 0.25 \text{ ns}$  [10]. The natural decay width  $\Gamma$  for this state, which is a function of the level lifetime  $\tau$  according to  $\Gamma = \hbar/\tau$ , is thus subject to a large degree of variation. As a result, integrated cross sections for the 934, 941 and 1078 keV levels cannot be accurately calculated. Instead, integrated cross sections can be directly measured, the results of which have been published by

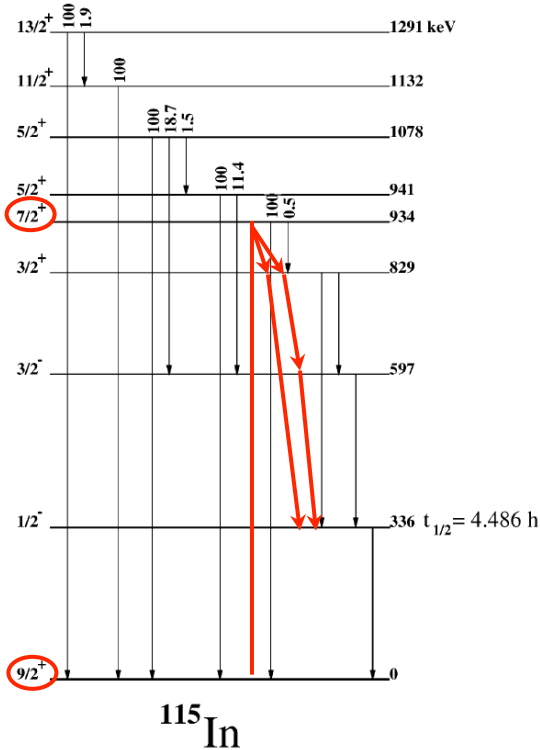


**Figure 26.** Simplified low-energy level scheme of  $^{115}\text{In}$ . The 336 keV isomer is fed by levels at 934 keV, 941 keV and 1078 keV in the  $^{115}\text{In}(\gamma, \gamma')^{115m}\text{In}$  reaction. The pathways involving the 934 keV level by which the isomer is fed are highlighted in red. Figure copyright 2001 Elsevier B.V. Reproduced with permission from [17].

Belic and others for the photoexcitation of the  $^{115m}\text{In}$  isomer [17]. The lowest energy integrated cross sections for this reaction are listed in Table 7.

**Table 7.** The lowest-energy intermediate states (IS) for photoexcitation of the  $^{115m}\text{In}$  isomer and their associated integrated cross sections (ICS) [17].

Intermediate state cross sections		Assigned levels	
$E_{IS}$ (keV)	ICS (ev·barn)	$E_x$ (keV)	$J^\pi$
940	$0.0084 \pm (0.0004)_{stat.} \pm (0.0023)_{syst.}$	934	$7/2^+$
		941	$5/2^+$
1085	$0.140 \pm (0.001)_{stat.} \pm (0.04)_{syst.}$	1078	$11/2^+$
1490	$0.78 \pm (0.06)_{stat.} \pm (0.21)_{syst.}$	1449	$9/2^+$
		1463	$7/2^+$
		1487	$9/2^+$
		1497	$7/2^+$

It is evident from this table that the LINAC must be capable of operating at a voltage greater than 940 keV to achieve any yield of  $^{115m}\text{In}$  from photoexcitation. Furthermore, the 1085 keV cross section is greater than that at 940 keV by a factor of 17, so a plot of yield versus beam energy would show a marked nonlinearity at this energy.

It is possible to determine the yield of the  $^{115m}\text{In}$  isomer created by photoexcitation from measurements of the decay activity of the indium sample following irradiation.  $^{115}\text{In}$  is nearly stable ( $t_{1/2} = 4.41 \times 10^{14}$  y), while its first isomeric state  $^{115m}\text{In}$  decays via emission of a 336 keV  $\gamma$ -ray to the ground state with a branching fraction of 45.8%. The isomer has a half life of  $t_{1/2} = 4.486$  h, so the activity is observable well after irradiation has ceased.

## 1.2 Hypothesis

The Dynamitron accelerator at WSU was used twice in the spring of 2014 to irradiate a sample of natural indium in separate attempts at achieving measurable amounts of  $^{115m}\text{In}$ . The  $\gamma$ -ray activities were measured with a 3"  $\times$  3" NaI(Tl) detector following irradiation times of 4.5 and 9.0 hours, respectively, with an operating voltage of 1.15 MV and beam current of 5  $\mu\text{A}$ . Neither experiment resulted in an identifiable 336 keV peak in the measured spectra.

A similar experiment was conducted at the Army Research Laboratory in Adelphi, MD, on 5 May, 2014, using a Varian L200A LINAC set at a nominal voltage 1.0 MV and 100  $\mu\text{A}$  beam current. In this experiment, a natural indium sample was irradiated for a period of 2.0 hours and  $\gamma$ -ray activity was measured using a high-purity germanium (HPGe) detector. The  $\gamma$ -ray spectra from the irradiated indium sample in the ARL experiment clearly showed a peak at 336 keV.

The results of these experiments suggest the energy calibration of either the

Dynamitron or Varian LINAC is in error. This hypothesis is partially supported by the results of a calibration of the Varian LINAC at ARL performed by Feroli and others in 2009 using a Compton-Hall voltmeter. The researchers concluded from this measurement that the LINAC operates at a voltage in excess of 1.2 MV at the nominal 1.0 MV setting [50]. Without measuring the electron beam energy or bremsstrahlung photon energy spectra directly, measurements of photoexcitation of the  $^{115m}\text{In}$  isomer allow one to verify the energy calibrations of the two accelerators. By comparing observed activities due to  $^{115m}\text{In}$  with the results of theoretical yield calculations, the calibration error on the affected accelerator can be estimated. This method was motivated by results published by L. Earwaker and D. Weaver, who used resonant nuclear reactions to diagnose faults in a Dynamitron at the Birmingham Radiation Centre, U.K. [51].

### 1.3 Experiment

The two experiments relevant to this discussion took place at ARL on May 5, 2014, and at WSU/AFIT on August 7, 2014.

#### **WSU/AFIT Experiment.**

In order to test the hypothesis, a measurable yield of  $^{115m}\text{In}$  had to be achieved with the Dynamitron, so the photoexcitation experiment was repeated at WSU. Following irradiation for 3.9 hours at a voltage of 1.2 MeV and a beam current of  $1.5 \mu\text{A}$ , the sample was transported to AFIT for measurement in a Canberra HPGe detector. This time, the  $\gamma$ -ray spectra taken after irradiation included a clear peak at 336 keV, likely due to the improved background suppression achieved with a copper-lined lead cave surrounding the detector. The  $\gamma$ -ray activity was sufficiently low (on the order of 1 Bq) that the peak would have been below the background

threshold if the sample were measured using an NaI(Tl) detector as before.

### Dynamitron.

The 1.5 MV Dynamitron at WSU cannot operate at voltages greater than 1.2 MeV, due primarily to vacuum system constraints. At 1.2 MV, the accelerator is capable of beam currents of approximately  $1.5 \mu\text{A}$ , which was the current used for the indium photoexcitation experiment.

### Converter and Target.

In order to maximize the flux of bremsstrahlung photons incident on the indium target, the converter assembly and 5.0 mm-thick natural indium (95.7%  $^{115}\text{In}$ ) foil sample were positioned at  $90^\circ$  to the incident electron beam. A typical Dynamitron target configuration is shown in Figure 27, with the converter and indium foil mounted against the copper cold head that forms the beam tube endcap. To minimize self-absorption, a converter was selected that consisted of the thinnest piece of tungsten (0.25 mm) immediately available.



**Figure 27.** Photograph of indium target and tungsten converter mounted on the copper cold head in the evacuated Dynamitron target chamber.

To eliminate the possibility of non-resonant nuclear excitation resulting from electron scattering in the indium, an aluminum spacer was needed between the tungsten and indium foils to absorb electrons that passed through the tungsten [19]. The minimum thickness of aluminum needed was determined using CASINO (version 3.2), a Monte-Carlo simulation program specifically designed to model the trajectories of electrons through solid materials [52]. The results of a CASINO simulation of 1000 electrons at 1.2 MeV (Figure 28) were used to determine that a 1.8 mm-thick piece of aluminum was sufficient to stop electrons from scattering into the indium target.

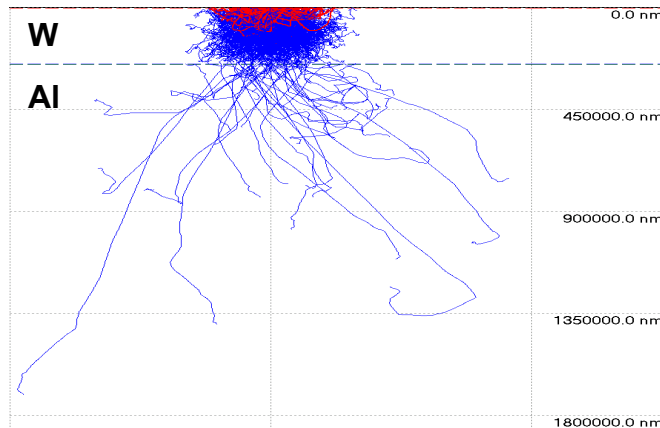


**Figure 28.** CASINO simulation to determine thickness of the tungsten converter and aluminum spacer necessary to stop electrons. The electron beam is incident from the top of the figure, while the vertical axis is penetration depth into the material. The blue lines represent the paths of the simulated electrons in the material, while the red lines are the characteristic X-rays from tungsten.

The aluminum separator ultimately used in the converter assembly was 3.1 mm thick, chosen based on the sizes of pieces immediately available for the experiment.

### Irradiation.

The indium sample was irradiated for a combined period of 3 hours, 55 minutes, using a voltage of 1.2 MeV and a beam current of 1.5  $\mu$ A. When operating at voltages in excess of 1.0 MeV, the corona current in the Dynamitron pressure vessel

underwent excursions that required the beam current to be decreased for short periods of time. Also, because of an inoperative cooling system, the Dynamitron had to be shut down approximately once per hour to cool the cold head assembly with ice. These two factors prevented the beam current from being maintained continuously at  $1.5 \mu\text{A}$ . However, an average beam-on electron flux of  $2.05 \times 10^{12} \text{ electrons/cm}^2\text{s}$  was calculated from the total charge shown on the current integrator at the cessation of irradiation. The beam-on and beam-off times were recorded and included in the yield calculations.

### **Sample Activity Measurement.**

Following irradiation, the indium sample was transported to AFIT for measurement in a Canberra HPGe detector. The time between beam off in the Dynamitron and the beginning of sample activity measurement was 23 minutes, which was incorporated into the yield calculations.

The HPGe detectors at AFIT sit in copper-lined lead caves for background suppression, and the detectors are integrated with Canberra's proprietary DSA-1000 high-voltage power supply / spectroscopy amplifier / multichannel analyzer (MCA). The DSA-1000 hardware interfaces with Genie 2000 software that runs on a desktop PC in the laboratory. The DSA-1000 incorporates pulse pile-up rejection (PUR) circuitry that discards signals due to pulse pile-up [43, 53]. Since the count rates were very low (on the order of  $1 \text{ s}^{-1}$ ), the PUR parameters were set to the minimum allowable values to avoid pulse rejection. Batch mode processing of the measured  $\gamma$ -ray spectra was not necessary for signal smoothing or further pile-up rejection, as the acquired spectra had sufficient definition to easily discern the 336 keV peak due to the presence of  $^{115m}\text{In}$  in the sample.

Before measuring the indium sample activity, the HPGe detector was calibrated

for energy and efficiency by measuring the  $\gamma$ -ray spectrum from a multinuclide planchette calibration source for 600 seconds. Present-day activities for each radionuclide in the source were calculated and input in Genie 2000 to perform a manual efficiency calibration, the results of which are shown in Figure 29.

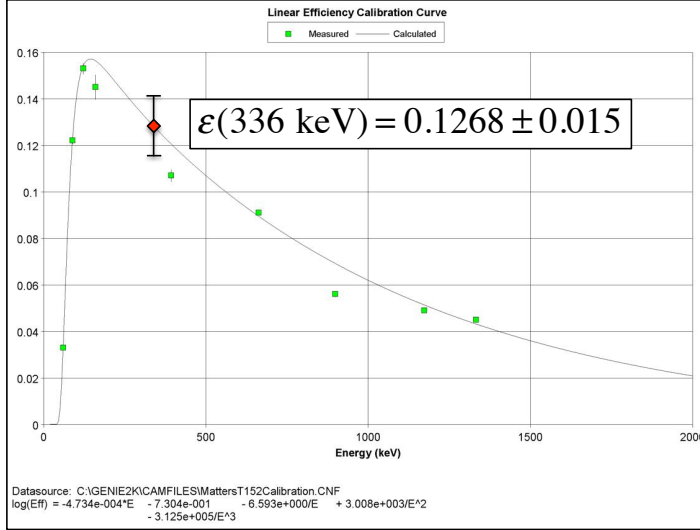


**Figure 29. Absolute detector efficiency curve resulting from calibration of the Canberra HPGe detector with a multinuclide planchette source.**

A least-squares fit was overlaid on the efficiency data to determine the HPGe detector efficiency at 336 keV, which was necessary for comparing experimental and theoretical yields.

Sample activities were on the order of picocuries, so hourly (3600-second live time) spectra were measured to ensure acceptable counting statistics. These hourly measurements were obtained over a period of 7 hours following irradiation, and a final spectrum was measured the following morning, 17 hours after irradiation ceased. The resulting peak counts were used to measure the half-life and initial activity of the  $^{115m}\text{In}$  in the sample (Figure 30).

Agreement between the measured half life and the  $t_{1/2} = 4.486$  hour value from literature confirmed that the decay of  $^{115m}\text{In}$  was the source of the 336 keV  $\gamma$ -ray peak.

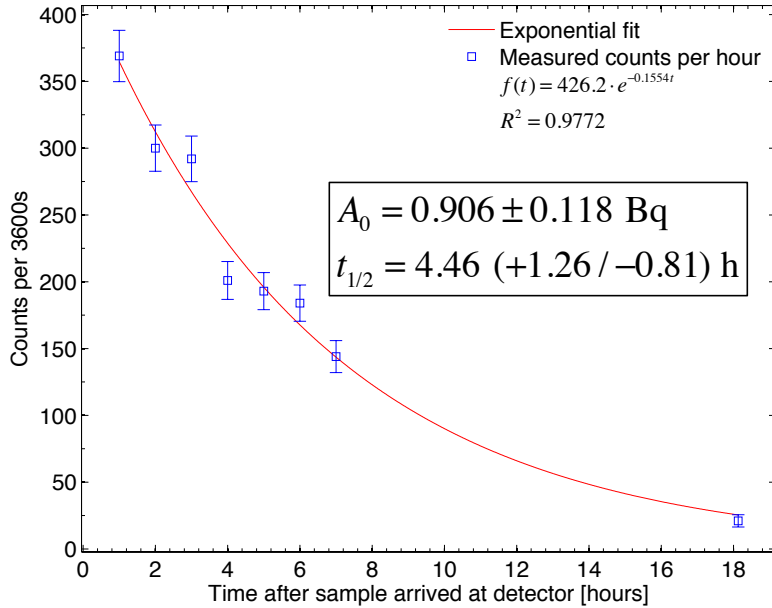


**Figure 30.** Hourly counts under 336 keV peak as measured in HPGe detector for the WSU/AFIT experiment. Fitting an exponential decay curve to the hourly peak counts allowed calculation of the initial activity  $A_0$  and half life  $t_{1/2}$ .

### ARL Experiment.

The 2 MeV Varian L200A electron LINAC at ARL was originally designed for industrial radiography applications. For this reason, a tungsten converter was incorporated in the LINAC at the electron beam terminus, similar to the configuration used in the Dynamitron. The higher electron energies achievable with the Varian L200A mandate the incorporation of a 0.84 mm thick tungsten converter [50].

The target, which consisted of a single 0.15 mm thick  $^{nat}\text{In}$  foil, was irradiated for a period of 2.0 hours at an operating voltage of 1.0 MV and current of 100  $\mu\text{A}$ , followed immediately by measurement of the sample activity in a background-suppressed HPGe detector for a live time of 3600 seconds. The absolute detector efficiency at 336 keV was 3.7%

## Comparison.

The 3600-second  $\gamma$ -ray spectra obtained from the first hour after irradiation in both experiments are compared in Figure 31.

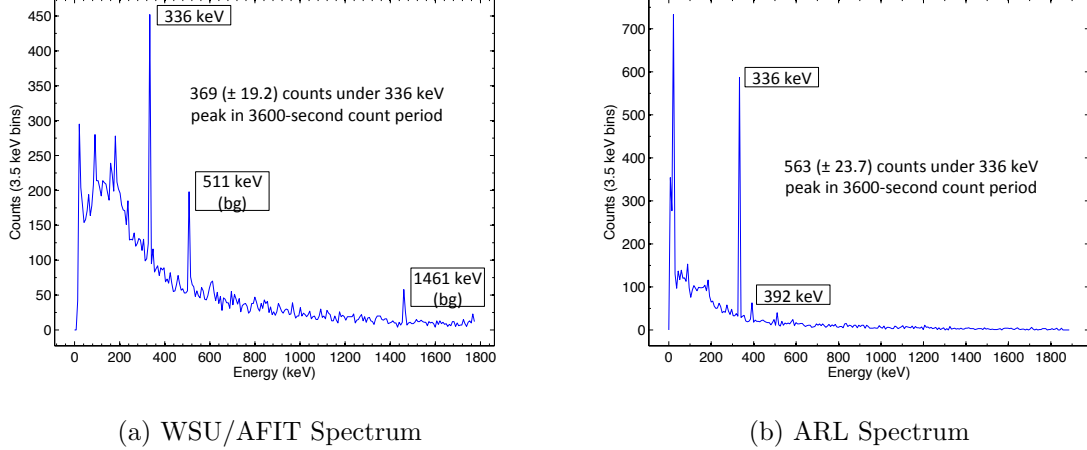


**Figure 31.** First hour  $\gamma$ -ray spectra obtained from measurement of irradiated indium samples from (a) WSU/AFIT experiment and (b) ARL experiment, both taken using background-suppressed HPGe detectors. Note the difference in vertical scales between the two plots. The 511 keV and 1461 keV peaks in (a) are background due to positron annihilation following pair production and environmental  $^{40}\text{K}$ . The small peak at 392 keV in (b) is due to the  $\gamma$ -decay of the  $t_{1/2} = 99.5$  hour isomer  $^{113m}\text{In}$ .

Notably, the ARL spectrum shows 53% more counts under the 336 keV peak, despite the fact that the indium target used in the WSU/AFIT experiment was 33 times thicker than that used in the ARL experiment.

## 1.4 Modeling Approach

In order to calculate a theoretical yield for the production of the isomer  $^{115m}\text{In}$ , one needs the spectral flux density  $\frac{d\Phi}{dE}$  of the photon source, from  $E = 0$  to the accelerator endpoint energy  $E_0$ , per Equation 7. The relative intensity at the resonant photon energy for the reaction is proportional to the total flux (a function of the beam current) and the integrated cross section of the appropriate resonant

transition, further explained in Section 2.5 of the thesis. The spectral flux density was simulated using GEANT4 instead of directly measured. Simulated photon energy spectra for the WSU/AFIT and ARL experimental configurations were used to calculate theoretical yields for photoexcitation of the  $^{115m}\text{In}$  isomer. These calculated yields were then compared with those obtained experimentally from measuring  $\gamma$ -ray activities with HPGe detectors.

### **GEANT4.**

GEANT4 was used to model both experiments to obtain spectral flux densities at the indium target locations. Both GEANT4 simulations used the same step, track, run and event action codes. For each bremsstrahlung photon that comes from outside the indium target volume and interacts within the target volume, these codes wrote the photon energy to a text file that was subsequently used to generate an energy histogram in Matlab. The detector construction and primary generator action codes were unique to each experiment, and varied according to beam energy and geometry.

### **WSU/AFIT Experiment.**

Using the accelerator, converter and target geometry described in Section 1.3, a C++ subroutine `DetectorConstruction.cc` was written to model the WSU/AFIT experiment geometry in GEANT4. With the subroutine `PrimaryGeneratorAction.cc` subroutine designed to simulate a 7.9 mm diameter beam, the code was run for approximately 6 days to simulate  $1 \times 10^9$  electrons at 1.2 MeV.

## **ARL Experiment.**

The Varian L200A geometry was modeled in GEANT4 to determine the photon flux incident on the indium foil sample. The ARL simulation was run for approximately 7 days to simulate  $1 \times 10^9$  electrons. The beam energy used in the simulation was 1.3 MeV, due to the conclusion of Feroli and others that the LINAC operating voltage was “greater than 1.2 MV” at the nominal 1.0 MV setting [50].

## **Spectral Flux Densities.**

The spectral flux densities obtained from GEANT4 were binned in 1 keV energy bins, the results of which are shown in the histogram plots of Figure 32. The majority of each plot was well-fitted by an exponential curve  $f(x) = a \cdot e^{bx}$ , but the tails of the two plots (energies  $\geq 0.9 \times E_0$ ) were nearly linear. The tails, which included the energies of the intermediate states, were therefore fitted using a linear function  $f(x) = a + bx$ , with  $R^2$  values of 0.9948 and 0.9932 for the WSU/AFIT and ARL spectra, respectively.

These curves were used to determine the flux at 940 keV and 1085 keV, which were then applied in the calculation of isomer yield.

## **1.5 Results and Analysis**

The photon flux at 940 keV and 1085 keV in the plots shown in Figure 32 were used with published integrated cross sections from Table 7 to calculate theoretical  $\gamma$ -ray activities due to the decay of  $^{115m}\text{In}$ . The initial activity  $A_0$  in decays/s, or Bequerels (Bq), when each indium sample arrived at the detector following irradiation is proportional to the yield achieved by photoexcitation, so it can be used as a basis of comparison between the theoretical and experimental results.

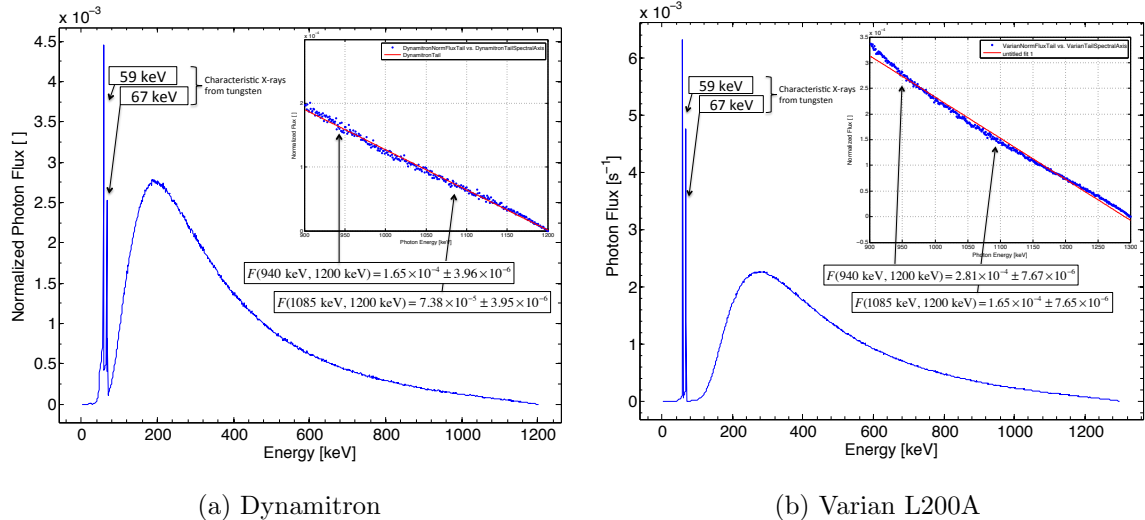


**Figure 32.** Modeled spectral flux densities from (a) WSU/AFIT and (b) ARL experiments. The peaks at 59 keV and 67 keV are characteristic X-rays from tungsten. The figures also identify the flux values at the energies for which the integrated cross sections are published.

### WSU/AFIT Experiment.

The theoretical and experimental results from the WSU/AFIT experiment showed agreement to within one standard deviation:

$$\text{Theoretical: } A_0 = 0.71 \pm 0.18 \text{ Bq}$$

$$\text{Experimental: } A_0 = 0.91 \pm 0.12 \text{ Bq}$$

The relatively close agreement between the theoretical and experimental results leads to the conclusion that any error in the Dynamitron energy calibration is not statistically significant.

## **ARL Experiment.**

The measured activity from the ARL experiment was nearly an order of magnitude less than the calculated activity, with a difference in excess of 3 standard deviations:

$$\text{Theoretical: } A_0 = 42.92 \pm 11.19 \text{ Bq}$$

$$\text{Experimental: } A_0 = 4.55 \pm 0.04 \text{ Bq}$$

The discrepancy between the theoretical and measured  $\gamma$ -ray activities suggest that either the current or the energy are in error on the Varian L200A accelerator. The possibility that the energy is less than 1.3 MeV is more probable than the current begin in error by a factor of 9.5.

Based on the results of this simulation, it is likely that the estimate of 1.3 MV for the Varian operating voltage is in error, and the actual value is closer to the nominal setting of 1.0 MV. Because the intermediate state at 1078 keV has an integrated cross section 16 times larger than the combined cross sections at 934 and 941 keV, the yield of  $^{115m}\text{In}$  is largely due to the 1078 keV intermediate state. At endpoint energies below 1078 keV, irradiation of the indium sample will produce a substantially lower yield of the  $^{115m}\text{In}$  isomer. Thus, a likely lower bound on the operating voltage of the Varian L200A is  $\sim 1.1$  MV.

## **1.6 Conclusion**

The results of the simulation and the WSU/AFIT experiment show that the theoretical and measured  $\gamma$ -ray activities due to the photoexcitation of  $^{115m}\text{In}$  agree to within a standard deviation, so there is no statistically significant error in the Dynamitron energy calibration. In contrast, the significant disagreement between theoretical and measured activities resulting from the ARL experiment is evidence

that suggests the Varian L200A energy was less than 1.3 MeV. At a nominal operating voltage of 1.0 MV, the results of the GEANT4 simulation suggest that the actual operating voltage  $V_{op}$  is in the range  $1.1 \leq V_{op} < 1.3$  MV. It is suggested that the Compton-Hall measurements described in [50] be repeated to obtain a more accurate estimate of the actual operating voltage for the Varian LINAC.

This experiment demonstrated that the Dynamitron at WSU is capable of achieving photoexcitation of nuclear isomers. However, its limited current of less than  $1.5 \mu\text{A}$  at operating voltages above 1 MV represents serious problem for future experiments involving nuclear isomers. To effectively perform nuclear structure investigations using  $(\gamma, \gamma')$  reactions, a radiation source should be able to produce currents of  $\geq 10 \mu\text{A}$  up to at least 1.2 MeV, and lower currents up to 1.5 MeV. An investment in radio frequency (RF) tuning the Dynamitron or improving the vacuum system may help achieve these gains. In-depth studies of nuclear isomers at WSU would also greatly benefit from the installation of a HPGe cave-type detector near the Dynamitron. This would reduce the transit time between irradiation and counting, which is essential for the study of isomers with short half lives.

## Bibliography

1. N. Fotiades, M. Devlin, R. O. Nelson, J. J. Carroll, and D. A. Matters, “Feeding of the  $J^\pi = 8^+$  isomer in  $^{186}\text{Re}$  in neutron-induced reactions,” Experiment Proposal to LANSCE/WNR Committee, 2014.
2. R. B. Firestone, *Table of Isotopes*. John Wiley & Sons, 2008. [Online]. Available: <http://ie.lbl.gov/toi.html>
3. K. L. Hainebach and D. N. Schramm, “Galactic evolution models and the rhenium-187/osmium-187 chronometer: A greater age for the galaxy,” *The Astrophysical Journal*, vol. 207, pp. L79–L86, 1976.
4. F. Käppeler, S. Jaag, Z. Y. Bao, and G. Reffo, “The  $s$ -process branchings at  $^{185}\text{W}$  and  $^{186}\text{Re}$ ,” *The Astrophysical Journal*, vol. 366, pp. 605–616, 1991.
5. S. E. Woosley and W. A. Fowler, “A nuclear correction factor for Re/Os cosmochronology,” *The Astrophysical Journal*, vol. 233, pp. 411–417, 1979.
6. M. Mosconi, “Re/Os cosmochronometer: Measurement of neutron cross sections,” 2007.
7. D. W. Seegmiller, M. Lindner, and R. A. Meyer, “ $^{186}\text{Re}$ : Nuclear structure and an isomer of half-life  $2 \times 10^5$  y,” *Nuclear Physics*, vol. A185, pp. 94–112, 1972.
8. P. M. Walker and J. J. Carroll, “Ups and downs of nuclear isomers,” *Physics Today*, pp. 39–44, June 2005.
9. Defense Science Board, “Radionuclide power to lighten the soldiers’ load,” in *Technology and Innovation Enablers for Superiority in 2030*, 2013, pp. 48–54.
10. Evaluated Nuclear Structure Data File (ENSDF). Brookhaven National Laboratory. [Online]. Available: <http://www.nndc.bnl.gov/ensdf/>
11. W. Greiner and J. A. Maruhn, *Nuclear Models*. Berlin-Heidelberg: Springer-Verlag, 1996.
12. P. Walker and G. Dracoulis, “High-spin nuclear traps,” *Physics World*, February 1994.
13. R. F. Casten, *Nuclear Structure from a Simple Perspective*, 2nd ed. New York, NY: Oxford University Press, 2000.
14. K. S. Krane, *Introductory Nuclear Physics*. Hoboken, NJ: John Wiley & Sons, 1987.
15. R. G. Lanier *et al.*, “Nuclear levels in  $^{186}\text{Re}$ ,” *Physical Review*, vol. 178, no. 4, pp. 1919–1948, February 1969.

16. P. Walker and G. Dracoulis, “Energy traps in atomic nuclei,” *Nature*, vol. 399, pp. 35–40, May 1999.
17. D. Belic *et al.*, “The new photoactivation facility at the 4.3 MV Stuttgart DYNAMITRON: Setup, performance, and first applications,” *Nuclear Instruments and Methods in Physics Research A*, vol. 463, pp. 26–41, 2001.
18. J. J. Carroll *et al.*, “Nuclear structure and depletion of nuclear isomers using electron linacs,” in *Application of Accelerators in Research and Industry*, vol. 1525, March 2013, pp. 586–594.
19. J. J. Carroll, Private Communication, 2014.
20. J. J. Carroll *et al.*, “Photoexcitation of nuclear isomers by  $(\gamma, \gamma')$  reactions,” *Physical Review C*, vol. 43, pp. 1238–1247, 1991.
21. G. D. Dracoulis *et al.*, “Connections between high- $K$  and low- $K$  states in the  $s$ -process nucleus  $^{176}\text{Lu}$ ,” *Physical Review C*, vol. 81, p. 011301, 2010.
22. J. M. Blatt and V. F. Weisskopf, *Theoretical Nuclear Physics*. New York, NY: Dover Publications, Inc., 1991.
23. T. Kibédi, T. Burrows, M. Trzhaskovskaya, P. Davidson, and C. Nestor. (2011, December) BrIcc v2.3S conversion coefficient calculator. [Online]. Available: <http://bricc.anu.edu.au/>
24. M. B. Chadwick *et al.*, “ENDF/B-VII.1 nuclear data for science and technology: cross sections, covariances, fission product yields and decay data,” *Nuclear Data Sheets*, vol. 112, no. 12, pp. 2887–2996, December 2011.
25. Evaluated Nuclear Data File (ENDF). [Online]. Available: <https://www-nds.iaea.org/exfor/endf.htm>
26. C. Wheldon *et al.*, “High-resolution particle spectroscopy of  $^{186}\text{Re}$ ,” *Journal of Physics G: Nuclear and Particle Physics*, vol. 36, pp. 95–102, July 2009.
27. A. G. Lerch, “Nuclear structure of rhenium-186 revealed by neutron-capture gamma rays,” Master’s thesis, AFIT-ENP-14-M-21. Graduate School of Engineering and Management, Air Force Institute of Technology (AU), Wright-Patterson AFB, OH, March 2014 (ADA598969).
28. GERmanium Array for Neutron Induced Excitations (GEANIE). Los Alamos Neutron Science Center. [Online]. Available: <http://wnr.lanl.gov/newwnr/4FP60R/About.shtml>
29. N. Fotiades *et al.*, “Measurement of  $^{238}\text{U}(n, xn\gamma)^{238}\text{U}$  partial  $\gamma$ -ray cross sections with GEANIE at LANSCE/WNR,” Los Alamos National Laboratory, Tech. Rep. LA-UR-01-4281, 2003.

30. N. Fotiades *et al.*, “Nuclear structure studies with GEANIE at the LANSCE/WNR facility,” in *International Conference on the Labyrinth in Nuclear Structure, Crete 2003*, ser. AIP Conference Proceedings, vol. 701, 2003.
31. N. Fotiades, Private Communication, 2014.
32. N. Fotiades, “GEANIE off-line data analysis,” LANSCE-NS, 2010.
33. S. A. Wender *et al.*, “A fission ionization detector for neutron flux measurements at a spallation source,” *Nuclear Instruments and Methods in Physics Research A*, vol. 336, pp. 226–231, 1993.
34. S. MacMullin *et al.*, “Neutron-induced  $\gamma$ -ray production cross sections for the first excited-state transitions in  $^{20}\text{Ne}$  and  $^{22}\text{Ne}$ ,” *Physical Review C*, vol. 86, p. 067601, 2012.
35. S. MacMullin *et al.*, “Partial  $\gamma$ -ray production cross sections for  $(n, xny)$  reactions in natural argon at 1-30 MeV,” *Physical Review C*, vol. 85, p. 064614, 2012.
36. H. Jin, “TSCAN (v2.6) and related programs,” ORNL, May 1995.
37. N. Fotiades, R. O. Nelson, M. Devlin, and J. A. Becker, “New levels and a lifetime measurement in  $^{204}\text{Tl}$ ,” *Physical Review C*, vol. 77, p. 024306, 2008.
38. N. Fotiades *et al.*, “Partial  $\gamma$ -ray cross section measurements in  $^{197}\text{Au}(n, xny\gamma\gamma)$  reactions,” 2003.
39. D. V. Perepelitsa, “( $n, n'\gamma$ ) reactions in  $^{63,65}\text{Cu}$  and background in  $0\nu\beta\beta$  experiments,” B.S. thesis, Massachusetts Institute of Technology, June 2008.
40. W. Younes, “GEANIE data usersub,” LANSCE-NS, December 1997.
41. D. Radford. RadWare. Oak Ridge National Laboratory. [Online]. Available: <http://radware.phy.ornl.gov/main.html>
42. Center for X-ray Optics and Advanced Light Source, *X-Ray Data Booklet*. Lawrence Berkeley National Laboratory, October 2009.
43. G. F. Knoll, *Radiation Detection and Measurement*, 4th ed. Hoboken, NJ: John Wiley & Sons, 2010.
44. T. Kibédi, T. W. Burrows, M. Trzhaskovskaya, P. Davidson, and C. Nestor, “Evaluation of theoretical conversion coefficients using BrIcc,” *Nuclear Instruments and Methods in Physics Research A*, vol. 589, pp. 202 – 229, 2008.
45. D. P. McNabb *et al.*, “Uncertainty budget and efficiency analysis for the  $^{239}\text{Pu}(n, 2n\gamma)$  partial reaction cross-section measurements,” May 2000.

46. T. Kawano, P. Talou, M. B. Chadwick, and T. Watanabe, “Monte Carlo simulation for particle and  $\gamma$ -ray emissions in statistical Hauser-Feshbach model,” *Journal of Nuclear Science and Technology*, vol. 47, no. 5, pp. 462 – 469, 2010.
47. K. Toshihiko, “Optical and Hauser-Feshbach statistical model code: CoH (ver. 3.3) manual,” CoH<sub>3</sub> Software Distribution, ver. 3.3, 2014.
48. A. J. Koning, S. Hilaire, and M. C. Duijvestjn. TALYS 1.6 user manual. [Online]. Available: <http://www.talys.eu/documentation/>
49. N. Fotiades, R. O. Nelson, M. Devlin, J. A. Becker, D. Dashdorj, R. A. Macri, and C. Y. Wu, “Partial  $\gamma$ -ray cross section and half-life measurements in  $^{205}\text{Tl}(n, xn\gamma)$  reactions,” Experiment Proposal to LANSCE/WNR Committee, 2008.
50. T. Feroli *et al.*, “Megavoltage bremsstrahlung end point voltage diagnostic,” *Review of Scientific Instruments*, vol. 80, p. 034301, 2009.
51. L. G. Earwaker and D. R. Weaver, “Diagnosis of Dynamitron accelerator faults through the observation of narrow nuclear resonances,” *Revue de Physique Appliquee*, vol. 12, no. 10, pp. 1419 – 1421, 1977.
52. R. Gauvin *et al.* CASINO: monte Carlo SImulation of electroN trajectory in sOlids. Universite de Sherbrooke, Quebec. [Online]. Available: <http://www.gel.usherbrooke.ca/casino/What.html>
53. DSA-1000 hardware manual. Canberra Industries. [Online]. Available: [www.qsl.net/k0ff/Genie/DSA-1000%20Hardware%20Manual.pdf](http://www.qsl.net/k0ff/Genie/DSA-1000%20Hardware%20Manual.pdf)

## Vita

Major David Matters grew up in San Jose, CA. He earned his commission as a second lieutenant in the Aviation Branch in 2004 from the University of San Francisco Army ROTC program before attending the Aviation Officer's Basic Course at Ft. Rucker, AL. He graduated from the Aviation Officer's Basic Course and rotary wing flight training in January 2006 as a rated pilot in the OH-58D(R) scout/attack helicopter. From 2006 to 2008, he served as an Assistant S3 and Platoon Leader in 1-25 Aviation Regiment (Attack) and 2-6 Cavalry Regiment at Wheeler Army Airfield, HI, and Kirkuk, Iraq. From 2008 to 2009, he served in the 3/25 Infantry Brigade Combat Team as an Assistant Brigade Aviation Officer and S3 Planner at Schofield Barracks, HI, and Tikrit, Iraq. Following completion of the Military Intelligence Captains' Career Course at Ft. Huachuca, AZ, in 2010, Major Matters commanded B Troop, 4-6 Attack Reconnaissance Squadron and served as the S3 of the 46th Aviation Support Battalion at Joint Base Lewis-McChord, WA. In 2013, he transitioned to Functional Area 52 (Nuclear and Counterproliferation) and entered the Air Force Institute of Technology in pursuance of a Master of Science degree in Nuclear Engineering.

Major Matters holds a Bachelor of Arts degree in Mathematics from the University of California, Berkeley, a Master of Arts in Mathematics from San Francisco State University, and a Master of Business Administration from Webster University. His awards and decorations include the Bronze Star (two awards), the Air Medal (three awards), the Meritorious Service Medal, the Army Commendation Medal (two awards), the Army Achievement Medal (two awards), and the Iraq Campaign Medal (three awards). He also holds the Aviator Badge, Air Assault Badge, and the Combat Action Badge. Following graduation, Major Matters will continue his academic studies at the Air Force Institute of Technology towards a Ph.D. in Applied Physics, with an anticipated graduation date of September 2016.

<b>REPORT DOCUMENTATION PAGE</b>					<i>Form Approved OMB No. 074-0188</i>
<p>The public reporting burden for this collection of information is estimated to average 1 hour per response, including the time for reviewing instructions, searching existing data sources, gathering and maintaining the data needed, and completing and reviewing the collection of information. Send comments regarding this burden estimate or any other aspect of the collection of information, including suggestions for reducing this burden to Department of Defense, Washington Headquarters Services, Directorate for Information Operations and Reports (0704-0188), 1215 Jefferson Davis Highway, Suite 1204, Arlington, VA 22202-4302. Respondents should be aware that notwithstanding any other provision of law, no person shall be subject to any penalty for failing to comply with a collection of information if it does not display a currently valid OMB control number.</p> <p><b>PLEASE DO NOT RETURN YOUR FORM TO THE ABOVE ADDRESS.</b></p>					
1. REPORT DATE (DD-MM-YYYY) 26-03-2015		2. REPORT TYPE Master's Thesis		3. DATES COVERED (From - To) Jun 2013 - Mar 2015	
4. TITLE AND SUBTITLE Analysis of the Nuclear Structure of Rhenium-186 Using Neutron-Induced Reactions		5a. CONTRACT NUMBER 5b. GRANT NUMBER 5c. PROGRAM ELEMENT NUMBER 5d. PROJECT NUMBER 5e. TASK NUMBER 5f. WORK UNIT NUMBER			
6. AUTHOR(S) Matters, David A., MAJ, USA					
7. PERFORMING ORGANIZATION NAMES(S) AND ADDRESS(S) Air Force Institute of Technology Graduate School of Engineering and Management (AFIT/EN) 2950 Hobson Way, Building 640 Wright-Patterson AFB, OH 45433-7765		8. PERFORMING ORGANIZATION REPORT NUMBER  AFIT-ENP-MS-15-M-098			
9. SPONSORING/MONITORING AGENCY NAME(S) AND ADDRESS(ES) Bill Ulicny, <a href="mailto:william.ulicny@dhs.gov">william.ulicny@dhs.gov</a> Department of Homeland Security – DNDO MGMT/OPO/Mailstop 0115 245 Murray Lane SW Washington, DC 20528-0115		10. SPONSOR/MONITOR'S ACRONYM(S) DHS – DNDO			
		11. SPONSOR/MONITOR'S REPORT NUMBER(S)  HSHQDC-14-X-00089			
12. DISTRIBUTION/AVAILABILITY STATEMENT Distribution Statement A. Approved for Public Release; Distribution Unlimited					
<b>13. SUPPLEMENTARY NOTES</b> <p>This material is declared a work of the U.S. Government and is not subject to copyright protection in the United States.</p> <p>Evaluated nuclear data for <math>^{186}\text{Re}</math> identify the majority of spin-parity assignments as tentative, with approximate values for the energies of several levels and transitions. In particular, the absence of known transitions that feed the <math>J^\pi = 8^+</math> isomer <math>^{186m}\text{Re}</math> motivates their discovery. This isomer, which has a half-life of <math>2 \times 10^5</math> years, has a potential application in an isomer power source. Additionally, the isomer's role in certain nucleosynthesis processes is not well understood, so measured cross sections for transitions that feed the isomer would have astrophysical implications. Using the GERmanium Array for Neutron Induced Excitations (GEANIE) spectrometer at the Los Alamos Neutron Science Center (LANSCE), (<math>n,2n\gamma</math>) and (<math>n,n'\gamma</math>) reactions in a 99.52% enriched <math>^{187}\text{Re}</math> target were used to obtain <math>\gamma</math>-ray spectra from <math>^{186}\text{Re}</math> and <math>^{187}\text{Re}</math>, respectively. The experimental data reveal 5 new transitions in <math>^{186}\text{Re}</math> and 4 new transitions in <math>^{187}\text{Re}</math>. Similarities between the level schemes of <math>^{184}\text{Re}</math> and <math>^{186}\text{Re}</math> suggest that one of the newly-observed transitions in <math>^{186}\text{Re}</math> feeds the isomer from a level at 414.9 keV. The <math>\gamma</math>-ray energy measured for this transition implies an isomer energy of 148.2(5) keV, which is a significant improvement over the adopted value of 149(7) keV.</p>					
<b>15. SUBJECT TERMS</b> Nuclear Structure, Neutron Inelastic Scattering, Rhenium-186					
16. SECURITY CLASSIFICATION OF:		17. LIMITATION OF ABSTRACT	18. NUMBER OF PAGES	19a. NAME OF RESPONSIBLE PERSON McClory, John W., Ph.D	
a. REPORT U	b. ABSTRACT U	c. THIS PAGE U	UU	113	19b. TELEPHONE NUMBER (Include area code) (937)255-6565 x7308